

# NA62e+: dark sector searches with high intensity positron beams in ECN3

F. Arias-Aragón<sup>a</sup>, L. Darmé<sup>b</sup>, R. Gargiulo<sup>e</sup>, G. Grilli di Cortona<sup>c</sup>, V. Kozhuharov<sup>g,h</sup>, E. Nardi<sup>a,d</sup>,  
M. Raggi<sup>e,f,g</sup>, T. Spadaro<sup>a</sup>, P. Valente<sup>f</sup>

<sup>a</sup>*Istituto Nazionale di Fisica Nucleare, Laboratori Nazionali di Frascati, Frascati, 00044, Italy*

<sup>b</sup>*Université Claude Bernard Lyon 1, CNRS/IN2P3, Institut de Physique des 2 Infinis de Lyon, UMR 5822, F-69622, Villeurbanne, France*

<sup>c</sup>*Istituto Nazionale di Fisica Nucleare, Laboratori Nazionali del Gran Sasso, Assergi, 67100, L'Aquila (AQ), Italy*

<sup>d</sup>*Laboratory of High Energy and Computational Physic, HEPC-NICPB, Rõvala 10, 10143, Tallin, Estonia*

<sup>e</sup>*Sapienza University, Department of Physics, Rome, 00185, Italy*

<sup>f</sup>*INFN, Sezione di Roma, Rome, 00185, Italy*

<sup>g</sup>*CERN, Geneva, Switzerland*

<sup>h</sup>*Faculty of Physics, University of Sofia "St. Kl. Ohridski", 5 J. Bourchier Blvd., 1164 Sofia*

---

## Abstract

Dark sector models present a rich phenomenology that requires high-intensity beams and precision detectors for thorough exploration. The NA62 experiment has already published several constraints on dark sector candidates, leveraging proton beam dump and meson decay techniques. This proposal seeks to significantly enhance NA62's discovery potential for dark sector candidates by using the positron-on-target technique. High intensity and high-energy positron beams, reaching up to  $\sim 150$  GeV energy, have already been produced at the SPS extracted beam lines. If a positron beam with an intensity in the range of  $2 \times 10^{14}$  positrons on target per year is delivered to the present K12 beam line, the NA62 detector would be ideal for searches of dark sector particles in both visible and invisible decay channels. Additionally, this approach would enable precision measurement of key standard model observable, including a detailed scan of  $\sigma(e^+e^- \rightarrow \pi^+\pi^-)$  and  $\sigma(e^+e^- \rightarrow \mu^+\mu^-)$  at the di-pion and di-muon production threshold, with discovery potential for the True Muonium ( $\mu^+\mu^-$ ) bound state.

---

## Contents

|           |  |           |
|-----------|--|-----------|
| <b>1</b>  | <b>Introduction</b>  | <b>3</b>  |
| <b>2</b>  | <b>The North Area beam lines and the NA62 detector</b>                     | <b>4</b>  |
| 2.1       | The K12 beam line . . . . .  | 4         |
| 2.2       | The NA62 experiment . . . . .  | 5         |
| <b>3</b>  | <b>Positron beams in ECN3</b>  | <b>5</b>  |
| 3.1       | Positron production rates in targets . . . . .                             | 6         |
| 3.2       | Separated and un-separated positron beams . . . . .                        | 7         |
| 3.3       | Separated and un-separated positron beams in K12 . . . . .                 | 7         |
| 3.4       | Separated and un-separated beams from T4 wobbling station . . . . .        | 8         |
| 3.5       | Positron energy range . . . . .  | 9         |
| 3.6       | Expected positron beam parameters . . . . .                                | 9         |
| <b>4</b>  | <b>Dark sectors at NA62e+ with a 75 GeV positron beam</b>                  | <b>11</b> |
| 4.1       | NA62 Luminosity with different target materials and thickness . . . . .    | 11        |
| 4.2       | Dark Photon production in positron-on-target collisions . . . . .          | 11        |
| 4.3       | Axion Like Particles production in positron-on-target collisions . . . . . | 13        |
| 4.4       | Dark sector particles decay modes . . . . .                                | 14        |
| <b>5</b>  | <b>Invisible decay searches techniques at NA62e+</b>                       | <b>14</b> |
| 5.1       | Missing mass: $e^+e^- \rightarrow \gamma X$ . . . . .                      | 15        |
| 5.2       | Missing momentum: $e^+N \rightarrow e^+NX$ . . . . .                       | 16        |
| 5.3       | Missing energy: $e^+Z \rightarrow e^+\cancel{E}$ . . . . .                 | 17        |
| <b>6</b>  | <b>Visible decay searches</b>  | <b>18</b> |
| 6.1       | Thin target: bump hunt . . . . .   | 18        |
| 6.2       | Long-living particles searches . . . . .                                   | 19        |
| <b>7</b>  | <b>Non minimal dark sectors</b>  | <b>22</b> |
| <b>8</b>  | <b>Standard model physics</b>  | <b>23</b> |
| 8.1       | Mesons photo-production and invisible mesons decays . . . . .              | 23        |
| 8.2       | The $e^+e^- \rightarrow \pi\pi$ cross section . . . . .                    | 24        |
| 8.3       | Study of the di-muon production cross section . . . . .                    | 24        |
| <b>9</b>  | <b>True muonium observation at NA62</b>                                    | <b>26</b> |
| 9.1       | Backgrounds discussion and detectors requirements . . . . .                | 26        |
| 9.2       | Monte Carlo Simulations . . . . .  | 27        |
| 9.3       | Discovery potential . . . . .  | 28        |
| 9.4       | Dedicated target setup: 16 target stations . . . . .                       | 28        |
| 9.5       | Parasitic setup with single target station . . . . .                       | 28        |
| <b>10</b> | <b>Conclusions</b>   | <b>29</b> |

## 1. Introduction

Accelerating primary high-energy positrons to the range of hundreds of GeV is a challenging and costly endeavor. In 2018, an Expression Of Interest (SPSC-EOI-018) was submitted to the CERN SPSC Scientific Committee for the development of a primary electron beam facility at the SPS accelerator. The project proposed generating an extracted high-intensity 16 GeV electron beam, after accelerating electrons into the SPS [1]. In contrast, secondary electron or positron beams, produced as by-products of proton collisions, can benefit from the existing high-energy proton machines at CERN and Fermilab. At the CERN's North Area (NA), extracted beam lines routinely produce electrons with energies  $\approx 100$  GeV from the 450 GeV protons of the SPS for the NA64 experiment [2]. However, the intensity and purity of the secondary positron beams have so far been the main limiting factors for positron-on-target experiments [3].

Positron-on-target collisions have proven to be an effective strategy for producing dark sector particles, thanks to the increased number of available production mechanisms, in particular the resonant annihilation of positron-electron into a dark sector boson [4]. More recently, it has been highlighted that the motion of electrons within high- $Z$  target materials allows experiments to significantly surpass the center-of-mass (c.m.) energy limit  $\sqrt{2m_e E_{\text{Beam}}}$  [5, 6] of annihilation-driven processes, which is typically imposed by the electron-at-rest condition in fixed-target experiments. In addition, the ability of associated production to enhance dark sector particle production rates in intermediate mass ranges makes positrons the preferred beam over electrons. Finally, to explore lepto-philic dark sector models, lepton-based production mechanisms are required, making searches with positron beams complementary to those based on protons.

In this paper, we will illustrate how high-energy and high-intensity positron beams can be delivered to the NA62 experiment in the CERN's ECN3 cavern, and how NA62 can achieve outstanding sensitivity to dark sector particles across a variety of scenarios.

Using a positron beam with a momentum of 80-100 GeV, NA62 will also be able of measuring the hadronic cross section in the  $\sqrt{s}$  range from 280 to 300 MeV, in which measurements at circular colliders are affected by particularly large statistical uncertainties. These cross sections, particularly  $\sigma(e^+e^- \rightarrow \pi^+\pi^-)$ , are well-known to be crucial theoretical inputs for the prediction of  $(g-2)_\mu$ .

By adjusting the positron beam to a slightly lower momentum of  $\sim 45$  GeV, the NA62 experiment will be able to make precise measurements of the cross section for  $e^+e^- \rightarrow \mu^+\mu^-$ , which has been proposed as a muon production scheme for the muon collider [7]. Additionally, during a dedicated run using a multi-target system and an upstream tracker, NA62 could potentially achieve the first observation of true muonium atoms, using techniques similar to the ones in [8].

## 2. The North Area beam lines and the NA62 detector

In this section, we will describe the key aspects of the K12 beam line and NA62 detectors that are relevant to the following discussion.

The ECN3 experimental hall, located 15 m underground, is part of the North Area complex, at the CERN Prevezin site. The complex is composed by a number of experimental facilities and lines making use of secondary and tertiary beams produced from the high-intensity proton beam extracted from the SPS; in particular ECN3 is served by the K12 beamline. After the slow extraction, the SPS 450 GeV protons are splitted in three branches by means of two beam splitters, towards three different targets: T2, T4, and T6, located in the TCC2 target hall (see Fig. 1). Primary protons not interacting in the T4 target are transported by the P42 transfer line over almost 900 metres to the T10 target located in the target hall TCC8. The T10 target is the starting point of the K12 beam line which delivers the high-intensity, unseparated secondary hadron beam to the NA62 experiment, located in the downstream experimental hall ECN3.

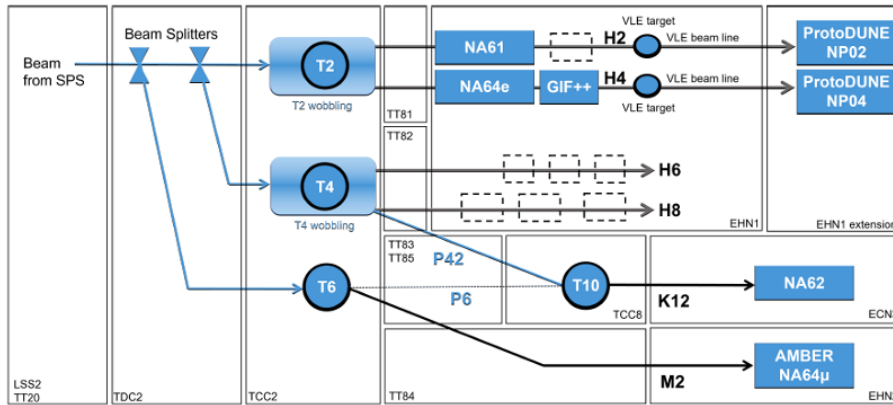


Figure 1: The schematic of the CERN North area extracted beam-lines [9].

A schematics of the CERN North Area beam lines is shown in Fig. 1. A more comprehensive description of the P42 and K12 beam lines can be found in [10].

### 2.1. The K12 beam line

The K12 beam line is located downstream of the P42 transfer line. It has been designed to provide a high intensity 75 GeV kaon beam to the NA62 experiment. Fig. 2 represents a schematic view of the K12 beam line. The K12 mixed hadron beam is produced by the interaction of the SPS primary 450 GeV protons with the T10 target made of 4x100 mm long beryllium rods.

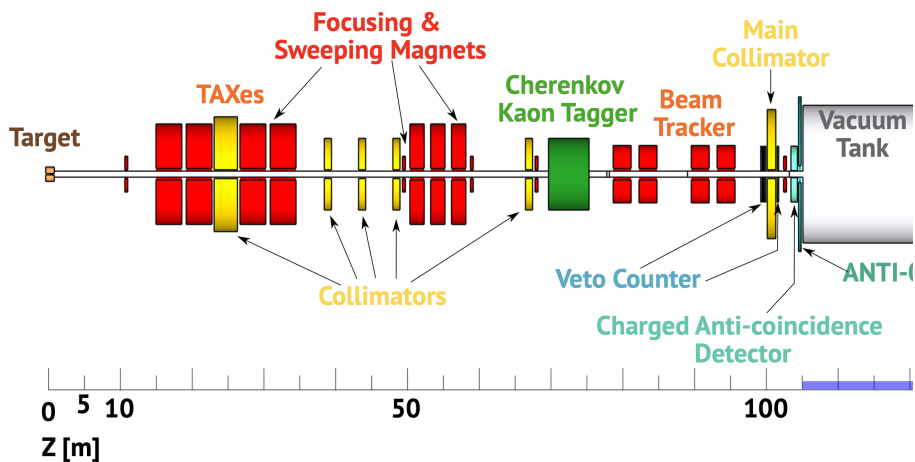


Figure 2: A schematic view of the K12 beam-line [11]

The beam is then focused by using a pair of dump collimators known as TAX (“Target Attenuator Experimental areas”) made of massive copper and steel blocks. A set of four strong

dipoles surrounding the TAX (the “first achromat”) ensures the selection of secondary particles with a momentum of 75 GeV and a 1.1% RMS resolution. Off-momentum and neutral particles are absorbed into the TAX. Positrons produced in the proton collisions are attenuated using a thin tungsten converter. After additional sweeping magnets and collimators are used to reduce muon halo, the kaon component of the unseparated hadron beam is identified by the KTAG Cherenkov detector. In the “second achromat” region, the beam is deflected vertically by a set of dipoles, and its momentum is measured by four silicon pixel detectors known as the GigaTracker with a resolution of 0.2%. A thorough description of the line can be found in [10].

## 2.2. The NA62 experiment

The NA62 experiment, located in CERN’s North Area, is a fixed-target experiment designed to measure the extremely rare decay  $K^+ \rightarrow \pi^+ \nu \bar{\nu}$ . With a branching ratio as small as  $8 \times 10^{-10}$ , this decay requires a background rejection on the order of  $\sim 10^{11}$  to be identified. To achieve this challenging goal, NA62 is equipped with high-precision, redundant detectors, which can be categorized into several groups:

- Particle Identification detectors: KTag, RICH, LKr calorimeter
- Photon veto detectors: LAV, LKr and SAC
- Charged particle veto detectors: CHANTI, MUV, HASC
- Energy and momentum measuring detectors: Lkr calorimeter and straw tracker

Kaon decays are reconstructed within a vacuum decay region over 70 meters long. The detector boasts an unprecedented photon and charged track rejection capability, below the  $1 \times 10^{-4}$  level, and enables precise measurement of the 4-momentum of both photons and charged particles. The particle identification system, consisting of the RICH detector, downstream calorimeters, and muon veto, allows for pion-muon separation down to the  $10^{-5}$  level.

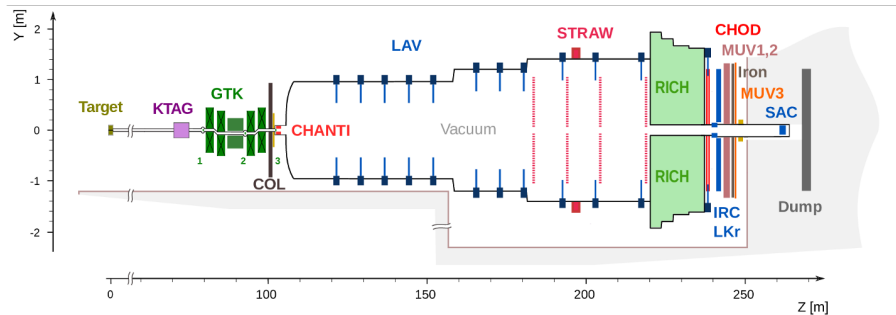


Figure 3: The NA62 experiment layout [12].

The layout of the detector is shown in Fig. 3. The NA62 detector has already been successfully employed for dark sector searches, both in kaon decays [13, 14] and in dump mode [15]. The current DAQ system can handle a Level 0 trigger rate of over 10 MHz, which is expected to be significantly higher with respect to positron mode operation requirements. A comprehensive description of the detector and its performance is beyond the scope of this paper, but more details on individual detectors and their performance can be found in [12].

## 3. Positron beams in ECN3

This section aims to outline potential strategies for delivering positrons to ECN3 and to provide a rough estimate of the number of positrons that could be delivered to the ECN3 cavern. We do not claim this estimate to be accurate beyond 50%-100%, as a more precise calculation is not necessary for this discussion. Optimizing production techniques and reducing hadron contamination will require a dedicated study by the CERN accelerator division. The figures presented here are intended only as indicative estimates of the positron flux for the subsequent physics case study.

### 3.1. Positron production rates in targets

To estimate the number of positrons that could be produced in ECN3, we begin with the annual proton delivery figures provided in the recent report “Post-LS3 Experimental Options in ECN3” [9]. In the last 3 rows of Tab. 1, we summarize the data from Table 1 of [9]. In the first line we added an estimate of the present maximum achievable proton flux based on the one achieved on T10 during the NA62 proton beam dump operation in 2024 and the number of spill delivered in 2024 run,  $\sim 600 \times 10^3$ .

|                          | Intensity on T10<br>[ $10^{13}$ p/spill] | $N_p$ /year<br>[ $10^{19}$ ] | $Ne^+$ /y<br>in $1\mu\text{ster}$ [ $10^{13}$ ] |
|--------------------------|--|------------------------------|---|
| NA62 ( $K^+$ )           | 0.55                                     | 0.33                         | 1.2   |
| HIKE phase 1.2 ( $K^+$ ) | 1.                                       | 0.72                         | 2.5   |
| HIKE phase 2.0 ( $K^0$ ) | 1.2                                      | 1.2                          | 4.2   |
| BDF                      | 4.0                                      | 4.0                          | 14  |

Table 1: Present and expected proton beam intensities (ppp) and positrons production rates per  $\mu\text{ster}$  in future ECN operations modes [9].

The next ingredient for our calculation is the positron yield per proton on target. Fig. 4 shows the positron rate obtained by using the TURTLE simulation program compared to measured values, as estimated experimentally at CERN in [16] for a 500 mm Be target, very similar to the present T4 or T10 targets.

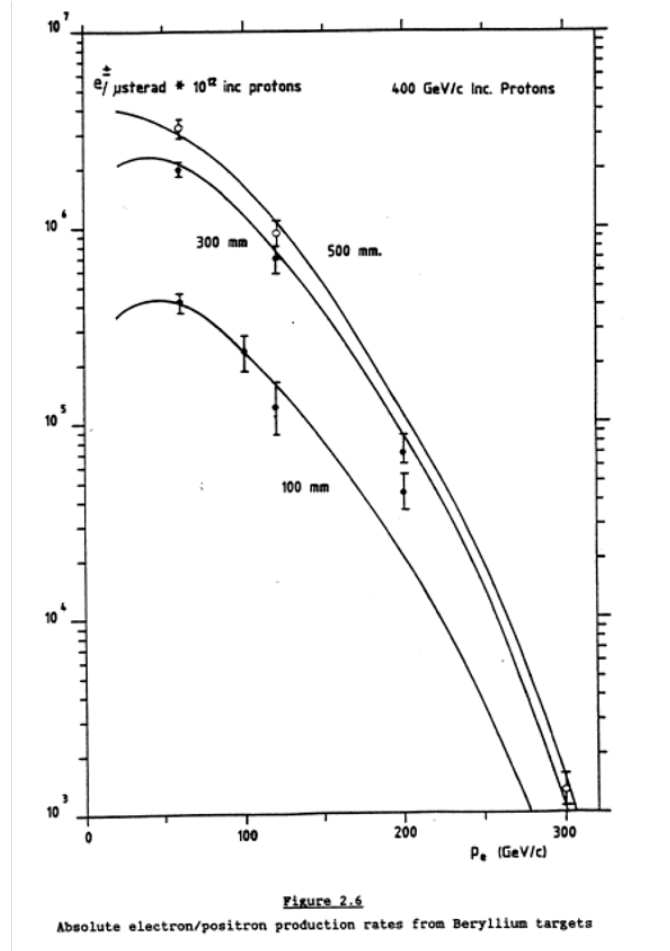


Figure 4: Absolute electron/positron production rates in  $1\mu\text{sterad}$  per  $1 \times 10^{12}$  400 GeV protons from Beryllium target [16]. Lines represents simulations while dots represent experimental measurements.

At the nominal K12 line energy of 75 GeV, the estimated yield is approximately  $3.5 \times 10^6$   $e^\pm/\mu\text{sterad}$ , which aligns well with measured values. This corresponds to a positron production probability per proton per  $\mu\text{sterad}$  of  $e^+/p = 3.5 \times 10^{-6}$ . Applying this probability, we obtain the

produced number of positron per year ( $N_{e^+}/y$ ) in a  $\mu\text{sterad}$  acceptance reported in the last column of Tab. 1

### 3.2. Separated and un-separated positron beams

Hadron beam contamination has been proven to be a crucial parameter in searching for dark sector particles in positron on target experiments [3]. Since the ‘70s, two main strategies were identified for producing positrons out of the SPS 450 GeV protons in the CERN North Area. The layout of generic beams obtained in the two configuration is shown in the left panel of Fig. 5.

The simplest one, producing a so-called “un-separated” positron beam, just exploits the natural positron yield obtained by colliding protons on a specific material. The dominant process is the production of  $\pi^0$  followed by the prompt  $\gamma\gamma$  decay. The photons from  $\pi^0$  decay convert within the target material or in a dedicated converter to produce  $e^+e^-$  pairs. The material type and thickness of the production target need to be optimized to maximize the positrons/hadrons ratio. In particular, the ratio radiation length over nuclear interaction length is the key parameter in the material choice, while positron production vs absorption determines the optimal converter thickness. Studies conducted at the NA extracted lines in the ‘80s concluded that 500 mm Be target is the optimal choice [16]. Despite producing very high intensity and being very easy to obtain, un-separated positron beams typically contain a maximum 30% of positrons at  $\sim 50$  GeV, which rapidly falls down below % level at higher momenta.

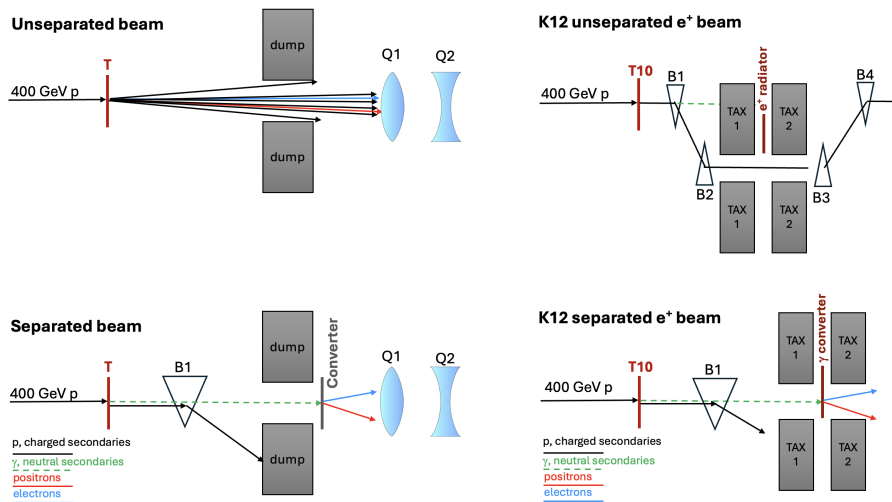


Figure 5: Left: scheme of un-separated and separated beams. Right: implementation in K12 beam line.

A much lower content of hadron can be obtained by using so-called “separated beams”. In this scheme, the un-separated beam obtained after the proton-on-target collisions is deflected by a bending magnet B1 towards a dump to eliminate all the charged secondaries. The photon component of the neutral beam is converted downstream the dump into  $e^+e^-$  pairs by a photon converter. These beams have typically a much lower intensity due to the small acceptance of the TAX holes and efficiency of the conversion target with respect to un-separated ones. In separated positive beams the hadron contamination is dominated by the protons from  $\Lambda \rightarrow p\pi^-$  decays. According to [3], the hadron contamination in a 75 GeV positive separated beam is  $\sim 1\%$  in the H4 beam line. Unfortunately, the value grows very rapidly with the beam energy reaching 100% at 150 GeV, strongly limiting the advantage of using positron-on-target technique in the NA64 experiment. Both schemes can be implemented in the first Achromat region of the K12 beam line as shown in Fig. 5, on the right.

### 3.3. Separated and un-separated positron beams in K12

The current 750 MHz 75 GeV un-separated hadron beam used by the NA62 experiment already contains a significant positron component estimated to be 8% in [10]. In Kaon operation mode, a tungsten radiator in between the two TAX modules allows to remove the positron component from the beam, as the positrons lose a lot of energy by Bremsstrahlung and are stopped in the second part of the beam line. Removing the radiator will allow  $> 50$  MHz of positron to reach the NA62 detector with just  $3 \times 10^{12}$  protons per pulse (ppp) The high particle flow is achieved by using a triplet of dipoles placed immediately after the target, which focuses the beam into the

TAX hole, resulting in an acceptance angle of up to  $42 \mu\text{sterad}$  [12]. According to our calculations based on [16], the positron's energy loss due to synchrotron radiation will unfortunately not allow significant hadron-to-electron separation in neither of the two achromats for energies below 150 GeV. The beam flux at 75 GeV is expected to be dominated by protons and pions, resulting in significant background in NA62. This can be partially mitigated by using the CEDAR as an electron tagger for low momentum beams, but a dedicated electron tagging system will be required for 75 GeV operation. The high rate in the detectors caused by hadrons, which dominate the beam content, will ultimately limit the maximum achievable positron rate.

To produce a separated positron beam, the operation of the K12 line needs to be slightly modified. The Tax1,2 holes must be aligned in the neutral beam configuration, and all bending magnets, except for Bend 1, need to be turned off. Bend 1 will deflect the charged secondaries toward TAX1, allowing only the neutral particles to be transmitted downstream. Unfortunately, the TAX holes have a very limited angular acceptance, which significantly reduces the positron flux compared to an unseparated beam. An existing motorized mechanism enables a 'radiator' made of tungsten plates of various thicknesses, ranging from 0 to 5 mm ( $1.3 X_0$ ), to be introduced into the beam. Originally intended to moderate the positron rate, this radiator can also be used as a photon converter. After passing through the radiators, the photons will be converted into a separated positron beam. In this configuration, no significant momentum selection is applied to the outgoing beam since the first achromat is not active. This could create additional problems for beam momentum measurement in the second achromat, as the beam spot may be larger than the GTK station size.

### 3.4. Separated and unseparated beams from T4 wobbling station

The most effective solution for producing a separated positron beam in CERN's North Area involves generating it at the T4 wobbling station (see Fig. 1) and transporting the secondary positrons through the P42 and K12 lines. Under these conditions, the positron beam will traverse the entire K12 line, including two achromats, allowing for proper momentum selection and muon sweeping. Additionally, the proton beam intensity at the T4 target is higher compared to T10, as the proton interactions at T4 cause significant attenuation.

The T4 target consists of five beryllium plates of varying lengths up to 500 mm [17]. In standard operation, the 100 mm Plate4 is currently used to optimize proton transport on the P42 beam line. To maximize positron production rates, the 500 mm-thick Plate1 needs to be used [17].

The T4 wobbling station, shown in Fig. 6, is perfectly suited for producing a separated positron beam. By increasing the magnetic field on the B3T bending magnet, the charged secondaries produced in the T4 collisions will be absorbed by the TAX, while neutral particles will pass through the TAX hole. The 500 mm Beryllium target configuration needs to be used to optimize production rate. The photons could be converted into  $e^+e^-$  pairs just between TAX and B1 magnet by introducing a motorized converter. The positrons will follow the path through P0, P42, and K12 lines to reach the NA62 experiment. This intervention on the B3T magnet B field should only slightly increase the energies and the intensity on the H8 and H6 lines, allowing for simultaneous operations of the test beam area.

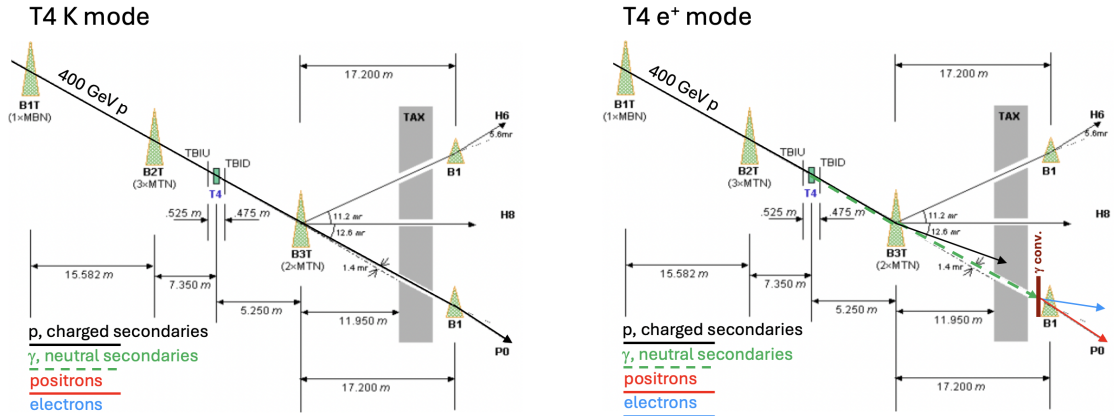


Figure 6: Layout of the T4 wobbling station in Kaon and positron mode [10]



Hadron contamination from meson decays will be minimal at any beam energy due to the 900-meter length of the P42 line, the distinct optics used for electron and proton transport, and the multiple changes in beam direction. Another advantage is that all protons delivered to T4 will contribute to positron production, while the transported beam will be a low-intensity positron beam, reducing the radiation concerns in P42 highlighted in [9]. Unfortunately, the positron flux is currently significantly constrained by the angular acceptance of the T4 hole for the photons. Finally, reverting to kaon operation mode is straightforward: simply restore the nominal magnetic field of the B3T bending magnet and remove the photon converter, go back to 100mm T4 to allow protons to reach the K12 line once again. A similar production scheme has been already implemented in the past in the E12 line [10] providing  $\sim 3 \times 10^7$  Hz of  $e^-/10$  GeV per  $1 \times 10^{12}$  protons with momentum exceeding 120 GeV [16].

On the other hand, a higher positron flux could be achieved by operating the line in unseparated beam mode, similar to the T4 kaon mode shown in Fig. 6. In this configuration, both primary protons, and secondary positrons and hadrons produced in the T4 collisions, will reach the P42 line. As with the unseparated case, the T4 TAX hole's acceptance currently limits the achievable positron rate. However, this rate can be significantly increased by using appropriate beam optics to focus the beam into the TAX holes. To reduce the hadrons content in the beam, the P42 optics could be tuned to favor positrons transport by leveraging their radiation losses, or a dedicated RF separation scheme could be implemented, albeit with some additional cost. Recently, a design featuring an upstream target and RF separation in P42 was proposed to produce a separated  $K^+$  beam for the HIKE experiment [18]. The primary limitation was the kaon lifetime, a constraint that would not exist with positron beams. Moreover, separating electrons from hadrons is considerably easier than separating kaons from hadrons, primarily due to the substantial synchrotron radiation emitted by positrons.

For both solutions a dedicated study of achievable positron rate in K12 and hadron contamination needs to be performed by the CERN accelerator division to identify the best and more cost-effective solutions.

### 3.5. Positron energy range

As shown in Fig. 4, positron production rates in proton-on-target collisions decrease significantly at high energies. Nevertheless, production rates up to approximately 1 MHz can be achieved for energies up to 200 GeV with around  $1 \times 10^{13}$  protons per pulse (ppp) on target. Conversely, intensity is not an issue for lower beam energy values. A negative hadron beam with 200 GeV energy has been delivered in 2007 to ECN3 for the NA62 RICH tests [19]. The maximum beam energy in the ECN3 cavern is currently limited by the bending power of the magnets installed in the K12 achromats. We expect the K12 line to be able to deliver positrons in the range 10-200 GeV without modifying the present K12 bending magnets [12, 20]. Expected energy spread after crossing the achromats can be as low as the percent level.

### 3.6. Expected positron beam parameters

In this section we summarize our estimates for the maximum ECN3 positron beam flux and other parameters. More precise estimates are necessary for designing an actual experiment, but the numbers used here are sufficiently accurate for the current discussion. To estimate the positron yield in the ECN cavern for various configurations, we must first define the geometry of the T4 wobbling station and the K12 line. For the separated beam, the yield is determined solely by the geometry, as the photons cannot be collimated. In contrast, for the unseparated beam, beam optics can be employed to significantly improve acceptance by focusing the beam into the TAX Hole.

|                  | TAX Hole size | D(target-hole) | Angular acceptance          |
|------------------|---------------|----------------|-----------------------------|
| T4 wobbling [17] | 20×40 mm      | $\sim 17$ m    | $\sim 1 \mu\text{sterad}$   |
| T10 target [12]  | 13 mm dia     | $\sim 22$ m    | $\sim 0.1 \mu\text{sterad}$ |

Table 2: Geometry and angular acceptance of the T4 and T10 target stations [12, 17].

Tab. 2 shows the current maximum angular acceptance of T4 and T10 targets, which have been used to obtain the predicted positrons flux. Tab. 3 summarizes expected rates of 75 GeV positron using the maximum primary protons flux,  $4 \times 10^{13}$  ppp, anticipated for the BDF scenario and  $600 \times 10^3$  spills/y. Scaling the positron rates in Tab. 3 by a factor of approximately 20 would enable achieving the current maximum rates, which align well with those obtained by the NA64 collaboration after accounting for the T2 angular acceptance. The exceptionally high positron flux

observed for the T10 unseparated beam is a result of the  $42 \mu\text{sterad}$  acceptance of the current K12 line. However, this configuration is unsuitable due to the total particle flux of few GHz being predominantly composed of hadrons.

Finally, we consider the effect of two possible modifications of the T4 wobbling station:

- T4 unseparated focused beam: install in T4 after the B3T dipole a focusing triplet similar to the one currently positioned just after the T10 target. We assume that this will enable an angular acceptance comparable with the one obtained for  $K^+$  in the current K12 line of  $\sim 42 \mu\text{sterad}$ .
- T4 separated 50 mm hole: drill a larger hole, 50 mm diameter, in the P42 entrance TAX increasing the photons angular acceptance to approximately  $2 \mu\text{sterad}$ .

| Beam configuration | $N_{e^+}/y$          | E range    | E Spread   | h fraction |
|--------------------|----------------------|------------|------------|------------|
| T4 unseparated     | $7.5 \times 10^{13}$ | 10-100 GeV | $\sim 1\%$ | few %      |
| T4 separated       | $5.0 \times 10^{13}$ | 10-100 GeV | $\sim 1\%$ | $< 1\%$    |
| T10 unseparated    | $3.5 \times 10^{15}$ | 10-100 GeV | $\sim 1\%$ | $> 80\%$   |
| T10 separated      | $7.3 \times 10^{12}$ | 10-100 GeV | 10%        | $\sim 1\%$ |
| T4 unsep. focused  | $3.5 \times 10^{15}$ | 10-100 GeV | $< 1\%$    | few %      |
| T4 sep. 50 mm hole | $1.5 \times 10^{14}$ | 10-100 GeV | $< 1\%$    | $< 1\%$    |

Table 3: Maximum positron beam parameters in ECN3 using  $4 \times 10^{13}$  pps and  $600 \times 10^3$  spill/y.

Tab. 3 shows that a focused, unseparated beam is the most effective solution for achieving high positron rates in ECN3. Producing the beam at T10 is impractical due to the high hadron content in the unseparated beam and the very low intensity of the separated one. In contrast, production at T4 offers the opportunity of significantly reducing the hadron content along the P42 line.

We choose as solution the unseparated focused beam produced at the T4 wobbling station, which we consider the best option for an experimental campaign. This setup provides maximum intensity, low hadron contamination, and a narrow momentum spread. However, our positron rate estimate for the unseparated focused beam from T4 is uncertain due to unknown factors, such as the angular acceptance of the P42 line after the installation of the focusing station and transportation losses along P42 line. Evaluating the feasibility and accurate positron yield of the proposed solutions, or exploring alternative and more effective approaches, is beyond the scope of this paper. These assessments require dedicated Monte Carlo simulations conducted by the CERN accelerator division.

Despite this, even if the positron flux were a factor of ten lower than the maximum value estimate in Tab. 3, it would still represent a unique opportunity for positron-on-target experiments. In this paper, we assume that a flux of  $2.0 \times 10^{14}$  75 GeV positrons on target, with hadron contamination reduced to  $\sim 1\%$ , can be delivered to NA62.

## 4. Dark sectors at NA62e+ with a 75 GeV positron beam

With a 75 GeV high-intensity positron beam in ECN3, the existing NA62 detector can support multiple dark sector search techniques simultaneously. Moreover, the beam's luminosity can be adjusted to match the detector's rate capability by selecting different target materials and thicknesses, optimized for specific dark sector scenarios. In the same experimental hall, target thicknesses can vary from a few hundred microns to several tens of centimeters (dump mode), thanks to the low radiation levels generated by  $\approx 10^{14}$  positrons on target per year ( $e^+OT/y$ ) at 75 GeV.

### 4.1. NA62 Luminosity with different target materials and thickness

We estimate the luminosity for two target scenarios: one using the existing 500  $\mu\text{m}$  thick silicon GiGaTracker3 station as the active target, and another using a 500  $\mu\text{m}$  tungsten target, either placed close to or significantly downstream of the GiGaTracker3 station to optimize detector acceptance. The 500  $\mu\text{m}$  thick tungsten target solution, previously proposed by the LDMX experiment [21], is complementary to the silicon target scenario. Low-Z and high-Z materials can enhance different contributions to the total cross section relative to specific backgrounds. The luminosity per year of data taking is computed as follows:

$$\begin{aligned} \frac{\text{NA62}_{\text{lumi}}}{y} &= \frac{e^+OT}{y} \frac{\mathcal{N}_A}{A} \frac{Z}{A} \frac{\rho}{D} \\ &= 46.7 \text{ pb}^{-1} \left( \frac{e^+OT/y}{2 \times 10^{14}} \right) \left( \frac{Z}{74} \right) \left( \frac{183.84 \text{ g/mol}}{A} \right) \left( \frac{\rho}{19.3 \text{ g/cm}^3} \right) \left( \frac{D}{0.05 \text{ cm}} \right). \end{aligned} \quad (1)$$

Here,  $e^+OT/y = 2 \times 10^{14}$  represents the number of positrons on target per year and  $D$  the target thickness in cm. This yields approximately  $6.7 \text{ pb}^{-1}/\text{year}$  for the silicon target and around  $47 \text{ pb}^{-1}/\text{year}$  for the tungsten target. Much higher positron flux or thickness of the targets will require major revision of the trigger and DAQ system of the NA62 experiment.

On the contrary, no rate issues are expected in dump mode, as the beam and all secondary interaction are fully absorbed by the dump itself. In this configuration, luminosity can be increased by a factor of approximately 100 by both raising the number of incoming positrons and increasing the target thickness to tens of centimeters, taking advantage of interactions from secondary particles produced in electromagnetic showers.

In order to illustrate the potential of such an experimental configuration in searching for light dark sectors, we will show the projected reach for two well-motivated new physics models, following the classification proposed in Ref. [22]. We will consider first a dark photon (DP) that interacts with the electromagnetic current via a coupling suppressed by a small kinetic mixing parameter  $\varepsilon$ . As a second candidate, we will consider axion-like particles (ALP), namely pseudo-scalars interacting with the photons via a coupling  $g_{a\gamma}$ , and with electrons via a coupling  $g_{ae}$ .

### 4.2. Dark Photon production in positron-on-target collisions

The interaction of a DP  $A'_\mu$  with a fermion  $\psi_f$  is described by the following Lagrangian:

$$\mathcal{L}_{A'} \supset -ig_V \bar{\psi}_f \gamma^\mu \psi_f A'_\mu. \quad (2)$$

This interaction holds also for DP models where the DP interacts with a SM fermion  $\psi_f$  via a kinetic mixing parameter  $\varepsilon = g_V/e$ .

In positron collisions on fixed targets, the dominant production modes for a DP  $A'$  are:

- a) Resonant annihilation:  $e^+e^- \rightarrow A'$
- b) Associated production:  $e^+e^- \rightarrow \gamma A'$
- c) Bremsstrahlung:  $e^+N \rightarrow e^+NA'$

The corresponding Feynman diagrams are shown in Fig. 7.

The first two production processes require positron beams, and offer a strong advantage in terms of production rates compared to electrons for DP masses around the resonant value  $m_{\text{res}} = \sqrt{2m_e E_{\text{Beam}}} \sim 277 \text{ MeV}$ . In particular, the resonant production mechanism has the highest cross-section due to a single electromagnetic vertex and Breit–Wigner enhancement. Unfortunately, this occurs only within a narrow mass range, very close to the  $\sqrt{s}$  of the collision. At lowest order, this process yields a cross section that, away from the resonant c.m. energy, is proportional to the  $A'$  width  $\Gamma_{A'}$ , which is strongly suppressed by the small coupling constant  $\varepsilon$  [4]

$$\sigma_{\text{res}} = \sigma_{\text{peak}} \frac{\Gamma_{A'}^2/4}{(\sqrt{s} - m_{A'})^2 + \Gamma_{A'}^2/4} \quad (3)$$

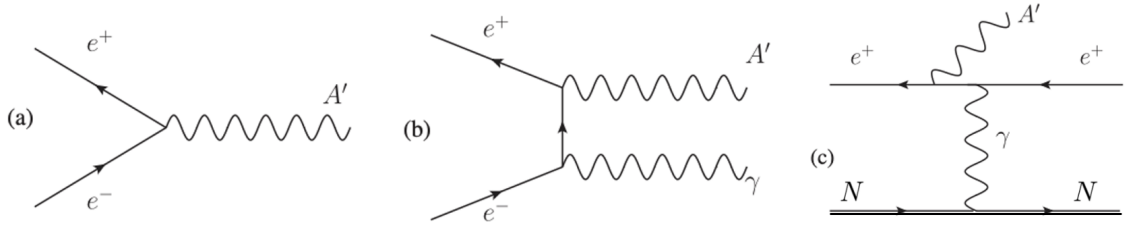


Figure 7:  $A'$  production mechanisms in electron-positron collisions [4]

where  $s$  is the invariant mass squared, and  $\sigma_{\text{peak}} = 12\pi/m_{A'}^2$  [4]. While the extremely narrow width of the DP makes this distribution strongly peaked around the resonant mass  $m_{\text{res}}$ , two main effects concur to widen significantly the mass range where this production mechanism dominates. First, the RMS beam energy spread  $\sigma_{\text{Beam}}/E_{\text{Beam}} \simeq 1\%$  is modeled using a Gaussian distribution, then further convolved with the differential track lengths  $\frac{\partial T_e}{\partial E}$  representing the total length (in unit of radiation length) of the material traversed by all  $e^\pm$  of a given energy  $E$  present in the shower. We use analytical expressions derived in [23]:

$$\frac{\partial T_e}{\partial E} = \int_0^{t_{\text{tar}}} dt I_e(t, E), \quad I_e(t, E) = \frac{1}{E} \frac{[\ln(E_0/E)]^{4t/3-1}}{\Gamma(4t/3)}, \quad (4)$$

where  $t_{\text{tar}}$  is the target length in unit of radiation length and  $E_0$  is the initial positron energy before entering the target.

Second, the atomic electrons in the target are not free nor at rest. Their spatial localization implies a certain momentum distribution, which in turn can alter significantly the CoM energy of the  $e^+e^-$  system. We model this effect following Ref. [5].

Finally, in the associated production case, the DP is produced alongside a Standard Model (SM) photon. Due to the initial-state radiation (ISR) photon, which modifies the collision's c.m. energy, the mass range for which associate production is effective is broader. The accompanying photon can be used to tag the invisible decay of  $A'$  and enables the measurement of its mass as the missing mass, calculated as  $M_{A'}^2 = (p_{e^+}^\mu - p_{e^-}^\mu - p_\gamma^\mu)^2$ . The total cross section as a function of the  $A'$  mass  $m_{A'}$  and of the coupling  $\varepsilon$  reads [24]

$$\sigma_{\text{ass}}(m_{A'}, \varepsilon) = \frac{8\pi\alpha^2\varepsilon^2}{s} \left[ \left( \frac{s - m_{A'}^2}{2s} + \frac{m_{A'}^2}{s - m_{A'}^2} \right) \log \frac{s}{m_e^2} - \frac{s - m_{A'}^2}{2s} \right], \quad (5)$$

where the c.m. energy of the collision is  $\sqrt{s}$ . The cross-section significantly increases when the mass of the particle is close to  $s$ , approaching the resonant value in the limit of vanishing photon energy. In practice, we merge both processes by keeping only the dominant one close to the resonant energy. The acceptance for this production process is high in NA62 due to the low photon emission angle caused by the high boost factor.

Finally, the dark bremsstrahlung process is similar to the SM bremsstrahlung one. In the so-called Weizsacker-William approximation [25, 26], we can write the integrated cross-section as

$$\sigma \approx \frac{4}{3} \frac{\alpha_{\text{em}}^3 \varepsilon^2 \mathcal{F} \beta_V}{m_V^2} \log \left( \frac{1}{(1-x)_c} \right), \quad (6)$$

where  $(1-x)_c = \max\left(\frac{m_e^2}{m_V^2}, \frac{m_V^2}{E_0^2}\right)$  and  $\frac{\alpha_{\text{em}} \mathcal{F}}{\pi}$  describes the effective photon flux (see, e.g. [27]). In practice, we obtain this cross-section numerically by means of the `MadGraph5_aMC@NLO` simulation framework [28], following the implementation of [27], using an effective  $NN\gamma$  interaction between the nuclei and the photon with form factor  $G_2$ . The form factor for a nucleus ( $Z, A$ ) is a function of the exchanged photon virtuality  $t$  and  $G_2(t) = G_2^{\text{el}} + G_2^{\text{in}}$  is defined by:

$$G_2^{\text{el}} = \left( \frac{a^2 t}{1 + a^2 t} \right)^2 \left( \frac{1}{1 + t/d} \right)^2 Z^2, \\ G_2^{\text{in}} = \left( \frac{a'^2 t}{1 + a'^2 t} \right)^2 \left( \frac{1 + \frac{t}{4m_p^2} (\mu_p^2 - 1)}{\left(1 + \frac{t}{0.71 \text{ GeV}^2}\right)^4} \right) Z, \quad (7)$$

with  $\mu_p = 2.79$ ,  $m_p = 0.938$  GeV the proton mass,  $a \equiv 111 \frac{1}{m_e Z^{1/3}}$ ,  $a' \equiv 773 \frac{1}{m_e Z^{2/3}}$  and  $d = 0.164 \text{ GeV}^2 A^{-2/3}$ .

### 4.3. Axion Like Particles production in positron-on-target collisions

A thorough study of production of Axion Like Particles (ALPs) in positron-on-target collisions can be found in [29]. In general, ALPs can interact both with photons and electrons via the couplings  $g_{a\gamma}$  and  $g_{ae}$  respectively, as described by the following Lagrangian:

$$\mathcal{L}_a \supset \frac{g_{a\gamma}}{4} a F^{\mu\nu} \tilde{F}_{\mu\nu} + \frac{g_{ae}}{2} \partial_\mu a \bar{e} \gamma^\mu \gamma_5 e, \quad (8)$$

where  $\tilde{F}_{\mu\nu} = \frac{1}{2} \varepsilon_{\mu\nu\rho\sigma} F^{\rho\sigma}$  with  $\varepsilon_{1230} = +1$  is the photon dual field strength tensor. Depending on the assumption on the dominant coupling of the ALPs to the SM, two different phenomenology of production and decay are obtained:

1. ALPs with dominant electron coupling ( $g_{ae} \neq 0$  and  $g_{a\gamma} \approx 0$ )
2. ALPs with dominant photon coupling ( $g_{a\gamma} \neq 0$  and  $g_{ae} \approx 0$ )

#### 4.3.1. ALPs with dominant electron coupling

The main production mechanisms for ALPs with dominant coupling to electrons  $g_{ae} \neq 0$  and  $g_{a\gamma} \approx 0$  are identical to the DP one shown in Fig. 7:

- a) Resonant annihilation:  $e^+ e^- \rightarrow a$ ,
- b) Associated production:  $e^+ e^- \rightarrow a \gamma$ ,
- c) ALP bremsstrahlung:  $e^+ N \rightarrow e^+ N a$ .

For this reason the detection techniques and the resulting limits can largely be obtained with the same procedure just by rescaling for the different production and decay rates. The cross section for resonant annihilation can be written straightforwardly after accounting for the beam energy spread as:

$$\sigma_{res}(m_a, g_{a\gamma}) = \frac{\sqrt{\pi} |g_{a\gamma}|^2 m_e}{4\sqrt{2}\sigma_E} e^{-\frac{(E_{res}(m_a) - E_B)^2}{2\sigma_E^2}}, \quad E_{res} = \frac{m_a^2}{2m_e} - m_e. \quad (9)$$

The ALPs associated production cross section in the hypothesis of dominant electron coupling reads [29]

$$\sigma_{ass}(m_a, g_{ae}) = \alpha_{em} g_{ae}^2 m_e^2 \frac{-2m_a^2 \beta s + (s^2 + m_a^4 - 4m_a^2 m_e^2) \log \frac{1+\beta}{1-\beta}}{2(s - m_a^2) s^2 \beta^2}, \quad (10)$$

where  $\beta = \sqrt{1 - \frac{4m_e^2}{s}}$ .

The cross section for ALP bremsstrahlung is obtained numerically using the same framework as for the DP case [29]. A simple order-of-magnitude estimate; accurate at around 10% can be straightforwardly obtained by dividing by two the DP result in Eq. (6), along with the replacement  $\varepsilon \rightarrow g_{ae} m_e / e$ .

#### ALPs with dominant photon coupling

The scenario is markedly different for models where ALPs exhibit dominant photon couplings, with  $g_{a\gamma} \neq 0$  and  $g_{ae} \approx 0$ . In this case the following production mechanisms are available :

- a) Resonant annihilation:  $e^+ e^- \rightarrow a$
- b) ALP-strahlung:  $e^+ e^- \rightarrow \gamma a$
- c) Photon fusion:  $e^+ e^- \rightarrow e^+ e^- a$  or  $e^+ N \rightarrow e^+ N a$
- d) Primakoff:  $\gamma N \rightarrow a N$

Among the various production mechanisms, ALP-strahlung, photon fusion, and Primakoff (see diagrams (b), (c), and (d) in Fig. 8) are the most significant in positron-on-target collisions.<sup>1</sup> These processes lead to distinct final states: ALP-strahlung produces a single photon and an ALP, while photon fusion results in an  $e^+ e^-$  pair along with an ALP. Primakoff production (d) relies on secondary photons generated in the electromagnetic shower and is particularly relevant in the thick-target scenario. We estimated both on-shell (Primakoff) and off-shell (photon-fusion)

<sup>1</sup>When the tree-level electron coupling vanishes, resonant production  $e^+ e^- \rightarrow a$  can still proceed via the loop diagram in Fig. 8 (a), and can be particularly relevant when the beam energy is tuned to the resonant value  $E_{res}$  and the beam energy spread  $\sigma_E$  is small, see Eq. (9). However, the effect of atomic electron momentum distribution that produces a smearing of the actual c.m. energy in the collision renders ineffective reducing the beam energy spread below  $\sim 1\%$  [4]. This effect is especially relevant in high  $Z$  materials as inner shell electrons can reach relativistic velocities [5, 6].

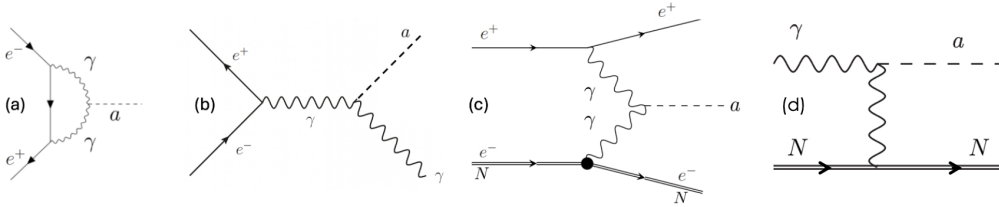


Figure 8: ALPs with dominant coupling to photons production mechanisms in positron-on-target collisions. [36]

processes with `MadGraph5_aMC@NLO`, using the same nucleus form factor as for DP bremsstrahlung. In both cases, if the momentum transferred to the nucleus by the virtual photon is smaller than the inverse of the nuclear size, the incoming positron interacts coherently with the whole nucleus, resulting in a cross-section enhancement by a factor of  $Z^2$ , where  $Z$  represents the atomic number of the nucleus [30]. Primakoff production strongly dominates due to the presence of multiple photons in the electromagnetic shower for thick targets. We additionally found an excellent agreement with existing analytical expressions [31] for the  $\gamma N \rightarrow aN$  process cross-section.

Additionally, even in the case of a vanishing axion-electron coupling at tree level, direct annihilation is possible via a loop-induced coupling (see diagram (a) in Fig. 8). In this case, we consider the following effective ALP-electron coupling for ALP production [32, 33]

$$g_{ae}^{eff} = \alpha g_{a\gamma} \frac{i}{4\pi m_e^2} (3A_0(m_e^2) + m_e^2 (2 - m_a^2 C_0(m_a^2, m_e^2, m_e^2, 0, 0, m_e^2))), \quad (11)$$

where  $A_0$  and  $C_0$  are the usual Passarino-Veltman functions that can be implemented using numerical packages like `LoopTools` [34, 35].

Accounting for the beam spread, the cross section for resonant  $e^+e^- \rightarrow a$  production is written as before, simply accounting for the effective coupling

$$\sigma_{res}(m_a, g_{a\gamma}) = \frac{\sqrt{\pi} |g_{ae}^{eff}(m_a, g_{a\gamma})|^2 m_e}{4\sqrt{2}\sigma_E} e^{-\frac{(E_{res}(m_a) - E_B)^2}{2\sigma_E^2}}, \quad (12)$$

while the associate production this time takes the following form [29]:

$$\sigma_{ass}(m_a, g_{a\gamma}) = \alpha g_{a\gamma}^2 \frac{(s + 2m_e^2)(s - m_a^2)^3}{24\beta s^4}. \quad (13)$$

Notably, when the tree-level electron coupling vanishes, the loop-induced coupling causes resonant production to dominate over ALP-strahlung within a narrow mass range, determined by the beam spread  $\sigma_{\text{Beam}}/E_{\text{Beam}} \approx 1\%$ . This range would expand further if electron motion were considered, as relativistic electrons in inner shells increase the available c.m. energy.

#### 4.4. Dark sector particles decay modes

If the dark sector is composed by more than one new particle, its internal structure will play an important role in fixing the relevant experimental signatures. The lightest dark sector particle, if unstable, will for instance typically decays back into SM particles, while heavier particles might experience semi-visible or fully-invisible decays patterns. Given that the dominant production modes for dark sector in NA62e+ are via lepton- or photon-driven processes, we will focus in this work on visible decays into lepton pairs for vector particles and photon pairs for ALPs.

Conversely, if additional light stable or very long-lived dark sector particles  $\chi$  exist with masses below half the  $X$  mass, the dark sector particle will predominantly decay invisibly into  $\chi\bar{\chi}$ , the so-called invisible decay scenario, which we study in the next section. Different combinations of production and decay modes lead to distinct experimental signatures. In the next section, we will show how NA62, with its versatile detector, can probe a large range of possibilities.

## 5. Invisible decay searches techniques at NA62e+

In this section, we assume that any dark sector particle  $X$  produced in positron-on-target collisions is either stable or primarily decays into lighter dark sector states  $\chi\bar{\chi}$ , which escape detection. In both cases, the final states are characterized by significant missing energy. This missing energy can be identified using different techniques, depending on the production mechanism. Figure 9 illustrates how the NA62 detector will be used to implement these techniques.

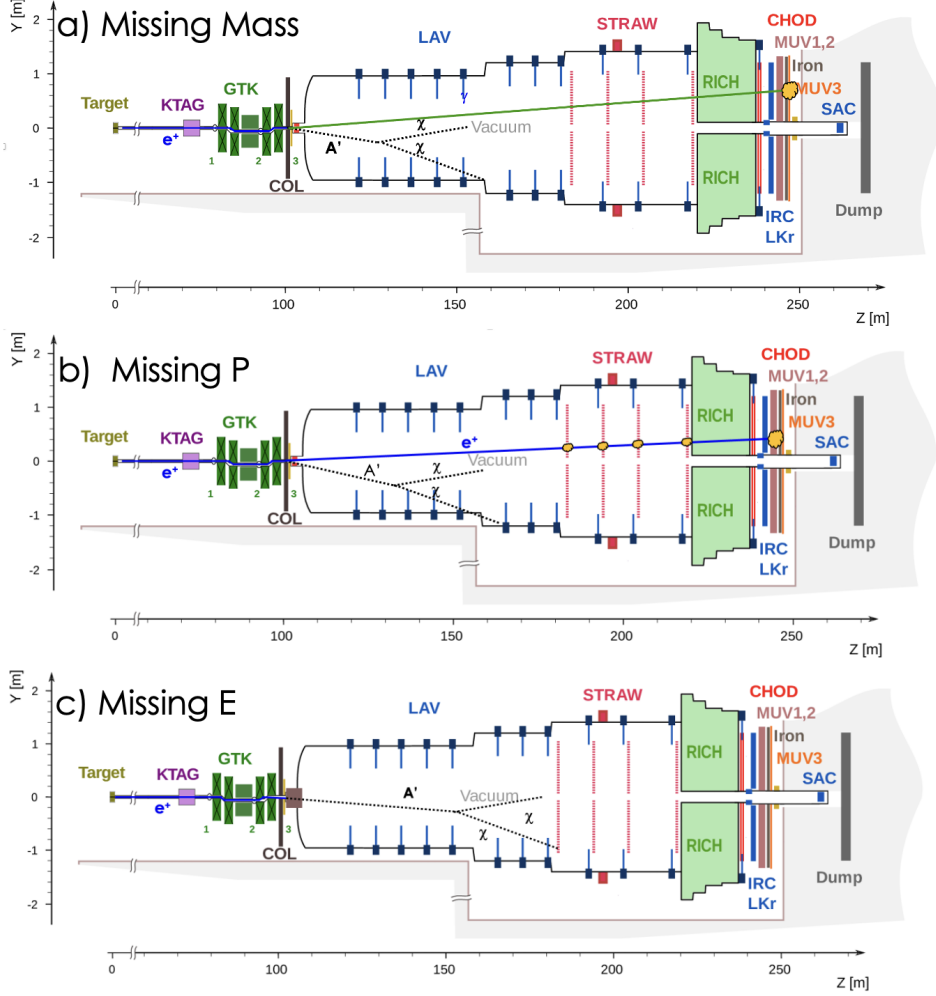


Figure 9: NA62e+’s invisible decay search techniques illustrated in the case of a DP  $A'$ . a) Missing mass b) Missing momentum c) Missing energy.

### 5.1. Missing mass: $e^+e^- \rightarrow \gamma X$

Mono-photon searches exploit associated production, measuring the SM photon’s four-momentum with the NA62 LKr calorimeter to infer the presence of an invisible particle. The GTK spectrometer precisely measures the incoming positron’s energy and direction, allowing for a precise determination of the missing particle’s invariant mass,  $M_X^2 = (p_{e^+}^\mu - p_{e^-}^\mu - p_\gamma^\mu)^2$ . A schematic view of the technique is given in Fig. 9 a). NA62’s excellent photon veto system enables nearly background-free searches, making it ideal for detecting DPs, ALPs, or very long-lived particles that decay invisibly or escape detection.

To compute the sensitivity of NA62e+ to the  $A'$  and ALPs invisible decays we used Eq. 5 and Eq. 10 for the cross section (CS)  $e^+e^- \rightarrow \gamma(A', a)$  for each mass values from 0 up to the kinematic limit  $M_{A',a}^{Max} = \sqrt{2 \times E_{Beam} \times m_e} \sim 277$  MeV. From the obtained CS values we estimated the 90% confidence level upper limit on the coupling  $\varepsilon$ ,  $g_{ae}$  as the Single Event Sensitivity (SES) for  $2 \times 10^{14}$  e+oT using the following formula:

$$UL(\varepsilon, g_{ae}) = \sqrt{\frac{2.3}{Acc_{A',a} \times CS \times NA62_{lumi}^{Si,W}}}. \quad (14)$$

The signal acceptance  $Acc_{A',a}$  was determined using the CalcHEP Monte Carlo generator [37] for different mass values. The  $A'$  model was implemented into CalcHEP and we applied an angular selection cut of  $1 \text{ mrad} < \theta_\gamma < 8.5 \text{ mrad}$  to the emitted recoil photon to ensure it would be detected by the NA62 LKr calorimeter. As a result, we found that  $\sim 15\%$  of the events are accepted by the calorimeter with a slightly increasing trend for higher masses. Additional acceptance gains can be explored using small-angle calorimeters to detect the recoil photon, provided the trigger rates and detector performance are adequate.

The single event sensitivity to  $A'$  invisible decays expected in NA62e+ are shown in Fig. 10. The filled areas represent existing limits from NA64 [2] (grey) and Babar [38] (green). The solid curves represent the expected Single Event Sensitivity (SES) for the mono photon analysis at NA62e+ with  $2 \times 10^{14}$   $e^+$ OT, using 500  $\mu\text{m}$  thick tungsten (red) and silicon (blue) targets, respectively.

Similar limits are obtained for invisible decays of ALPs with dominant coupling to electrons shown in Fig. 11. We used as in the DP case the zero background approximation and a 15% acceptance, estimated using CalCHEP [37].

Profiting by the higher production rates provided by the associated production at high mass compared to  $A'$  bremsstrahlung, NA62e+ can improve up to 2 orders of magnitude the present limits by NA64 in the mass region 150–277 MeV for both  $A'$  and ALPs invisible decays. Moreover, several different regions of parameters space can be probed by simply changing the positron beam momentum. Pushing the beam energy to 150 GeV, as in the NA64 case, the kinematical limit for the single photon analysis will reach the 400 MeV region. The lower positron flux at higher energy can be compensated by increasing the target thickness. The high energy scenario, however, might require significant improvement in the bending power of the K12 achromat magnets and is therefore not yet considered in Fig. 10.

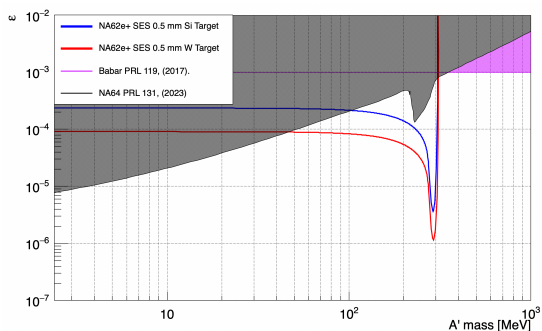


Figure 10: Expected NA62e+ sensitivity to  $A'$  invisible decays in different scenarios. Blue line Silicon and red line tungsten target in single photon mode. Filled grey area represents NA64 [2] and filled green one the Babar [38] limits.

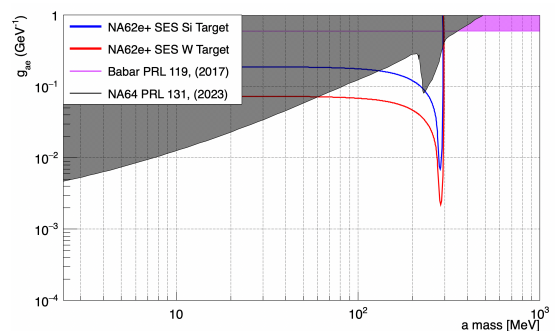


Figure 11: Expected NA62e+ sensitivity to ALPs ( $g_{ae}$ ) invisible decays in different scenarios. The blue (red) line represents a silicon (tungsten) target in single photon mode. The shaded gray area shows the NA64 limits [2], and the green one the BaBar limits [38].

Finally, the motion of atomic electrons, particularly in the tungsten target, can significantly enhance the  $A'$  production rates to masses beyond the kinematic limit of the electron-at-rest approximation [5]. However, its effect on the missing mass resolution has not yet been calculated, and we therefore do not include it in the projected reach shown in Figs. 10 and 11. We nonetheless note that it is expected to be negligible in Si compared to tungsten target.

## 5.2. Missing momentum: $e^+N \rightarrow e^+NX$

The missing momentum experiment exploits the bremsstrahlung  $X$  production mechanism. In this process, the dark sector particle is emitted from a primary positron after interacting with a target nucleus. The  $X$  subsequently decays into invisible particles, leading to a significant reduction in the final-state positron's momentum compared to its initial value. The measurement of the  $e^+$  momentum reveals a significant difference from the original beam momentum. A schematic view of this technique is shown in Fig. 9 b). This technique, proposed for the first time for the LDMX experiment [39], is considered the one with lowest background and has not been used until now. To conduct such an experiment, both an upstream tracker before the target and a recoil tracker after the target are essential. In the NA62 experiment, the GTK system serves as the upstream tracker, providing a 0.2% precise measurement of the incoming positron's momentum. The straw spectrometer, acting as the recoil tracker, offers a  $\sim 1\%$  precision measurement of the recoil momentum.

The NA62 experiment is designed as a missing momentum experiment. Notably, the decay  $K^+ \rightarrow \pi^+\nu\bar{\nu}$  involves a missing momentum final state, closely resembling the process  $e^+ \rightarrow e^+A' \rightarrow e^+\chi\bar{\chi}$ . Compared to LDMX, NA62 offers the capability to reconstruct the invariant missing mass and features a very precise particle identification (PID) system, which enhances background rejection, particularly against hadronic final states. The high energy of the incoming positrons assure the complete angular coverage of photon veto detectors for SM backgrounds. The capability of obtaining very high rejection factor on extra particles has been demonstrated in the recent measurement of the  $BR(K^+ \rightarrow \pi^+\nu\bar{\nu})$  [40]. The NA62e+ sensitivity shown in Fig.12



has been obtained assuming 0 background and applying a conservative missing momentum cut of 50%. The limit was calculated using Eq. 14 in which  $Acc$  and  $CS$  have been obtained using

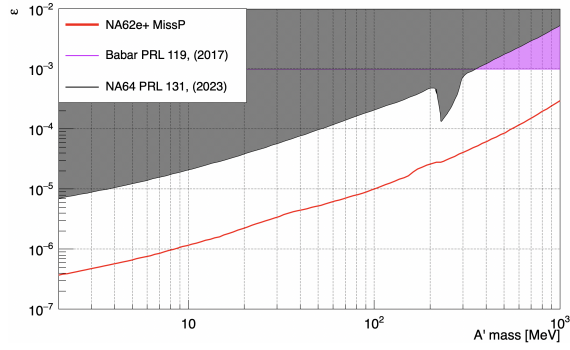


Figure 12: NA62e+ missing momentum sensitivity to invisible  $A'$  decays (red) compared to existing limits.

MadGraph5\_aMC@NLO [28] as described in Sec. 4.2. The acceptance was calculated ensuring that the recoils positron lies into the spectrometer acceptance ( $1 \text{ mrad} < \theta < 8.5 \text{ mrad}$ ). A very similar acceptance to the case of mono-photon  $\sim 15\%$  has been obtained.

### 5.3. Missing energy: $e^+Z \rightarrow e^+\mathcal{E}$

In the missing energy technique an active thick target absorbs and measures the incoming positron. If in the interaction a dark sector state  $X$  is produced, the measured energy differs significantly from the incoming positron momentum. A missing energy search can potentially be performed at NA62e+ installing an active target downstream the GTK3 station, shown in brown in Fig. 9 c), and using the rest of the NA62 detector as a global veto system.

The NA64 experiment has extensively demonstrated the effectiveness of the missing energy technique using an electron beam on target. From 2016 to 2022, NA64 accumulated  $9.37 \times 10^{11}$  100 GeV electrons on target, achieving the most stringent limits on invisible DP decays [2]. A similar search using positrons, as proposed in the POKER project, has also been undertaken by the NA64 collaboration. However, to date, only a limited amount of data,  $1 \times 10^{10}$  positrons on target at 100 GeV, has been collected in this mode [41]. In positron dump mode, NA62e+ has the potential to accumulate more than 1000 times the number of positron collisions compared to NA64[41], leveraging the high proton flux enabled by the North Area BDF upgrades. With minor interventions, a 50 cm long active target system, similar to POKER calorimeter [42], can be installed in the NA62 experiment, downstream the GTK region, enabling missing energy measurements. This configuration will allow profiting from all the three production mechanisms provided by positron beams leading to the maximum sensitivity to invisible decays. The achievable exclusion limits with  $2 \times 10^{14} e^+oT$ , assuming no background, are shown in Fig. 13 for  $A'$  searches.

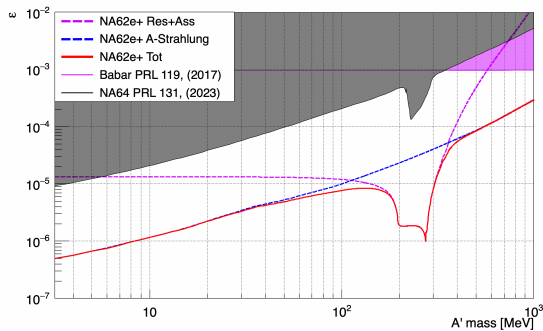


Figure 13: NA62e+ missing energy sensitivity to invisible  $A'$  decays (red).

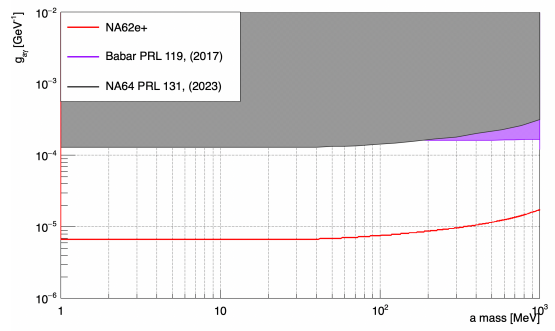


Figure 14: NA62e+ missing energy sensitivity to invisible  $a$  decays (red).

The dashed blue line represents the contribution from  $A'$ -bremsstrahlung, which is dominant at low masses. The production rate for this contribution has been obtained using MadGraph5\_aMC@NLO [28], accounting for the interaction in the whole target thickness and including a 50% missing energy. The violet dashed line shows the contribution of resonant and associated production, including interaction of the primary positrons and the contribution of secondary positrons generated in

the electromagnetic shower obtained following the prescription in [43]. In this configuration, the limits from NA62e+ can surpass existing limits by more than one order of magnitude in a mass range from 0 to 1 GeV, and by more than two orders of magnitude in the resonance-dominated region [200 MeV - 300 MeV]. According to [44] additional sensitivity will be provided by invisible decays of photo-produced light mesons  $\rho$ ,  $\omega$ ,  $\phi$ . Mesons decay will improve the reach of NA62e+ experiment for  $m_{A'} > 500$  MeV region in which  $A'$ -strahlung is weak, due to the  $1/m_{A'}^2$  suppression of the cross section.

In the case of ALPs with photon-dominated coupling ( $g_{a\gamma}$ ), the sensitivity was computed by considering ALP-strahlung and Primakoff production (diagrams (b) and (d) in Fig. 8) while also accounting for a 50% missing energy probability. The results, presented in Fig. 14, show that sensitivity is primarily driven by Primakoff production across the entire mass range. The NA62e+ sensitivity (red) is compared to the exclusion limits from [29], with the NA64 result (grey) rescaled to reflect the additional statistics collected by NA64 [3] relative to [29]. Notably, the NA62e+ sensitivity significantly surpasses that of NA64 and BaBar up to a few GeV in mass.

## 6. Visible decay searches

The visible decay model assumes that the produced dark sector particle  $X$  decays mostly into SM particles. We further assume a 100% branching ratios into SM leptons (or photon pairs for ALPs in the mass range we are interested in). Due to its small coupling to the SM leptons, the  $X$  particle will exhibit a relatively long-lifetime that can result in decay vertices significantly displaced with respect to the production target thanks to the  $\approx 1000$  boost factor provided in NA62e+ by the 75 GeV beam energy.

The NA62 detector is equipped with a spectrometer to measure the momenta and directions of charged particles and a LKr calorimeter to determine the energies of photons, enabling the full reconstruction of visible decays of dark sector particles. Additionally, a decay vertex position resolution  $\approx 0.5$  m is achievable, allowing NA62 to distinguish long-lived particle decays from SM background.

Fig. 15 illustrates the various techniques for detecting visible final states at NA62e+. In panels a) and b), the final state is obtained by considering only  $A'$  bremsstrahlung production. Similar searches, originated by associated production where a photon replace beam positron as final state particle, can also enhance the sensitivity. In dump mode, panel c), the accompanying particle is irrelevant as it is absorbed by the dump itself.

### 6.1. Thin target: bump hunt

The bump-hunting technique, illustrated in panel a) of Fig. 15, is employed to search for resonances within a smooth background. In this approach, a dark-sector particle produced at the target promptly decays into Standard Model particles. The reconstructed invariant mass is expected to exhibit a distinct peak superimposed on the smooth background distribution. Several final states are available in a positron-on-target experiment depending on the production mechanism and the exotic particle decay of interest. In the case of NA62e+, we assume that the dominant decays are to lepton pairs, as hadronic decays are sub-dominant in this mass range. Limiting thus our analysis to leptonic decay products, the final state generated by both  $A'$  and ALPs with dominant electron couplings are:

- a)  $e^+e^- \rightarrow X \rightarrow e^+e^-$  or  $e^+e^- \rightarrow X \rightarrow \mu^+\mu^-$
- b)  $e^+e^- \rightarrow \gamma X \rightarrow \gamma e^+e^-$  or  $e^+e^- \rightarrow \gamma X \rightarrow \gamma \mu^+\mu^-$
- c)  $e^+N \rightarrow e^+NX \rightarrow Ne^+e^+e^-$  or  $e^+N \rightarrow e^+NX \rightarrow Ne^+\mu^+\mu^-$

In all the cases mentioned, a pair of leptons will be reconstructed by the NA62e+ spectrometer, enabling the computation of their decay vertex and invariant mass. In case the dominant coupling of an ALP  $a$  is to photons, one has the following final states:

- d)  $e^+e^- \rightarrow a \rightarrow \gamma\gamma$
- e)  $e^+e^- \rightarrow \gamma a \rightarrow \gamma\gamma\gamma$
- f)  $e^+e^- \rightarrow e^+e^-a \rightarrow e^+e^-\gamma\gamma$
- g)  $e^+N \rightarrow e^+Na \rightarrow Ne^+\gamma\gamma$

Acceptance has been evaluated to be 15% for associated production and prompt decay and it's expected to be similar in the other cases, ensuring good detection capability for all the decay channels. The main source of background for visible  $A'$  searches is the Bhabha scattering process, whereas for ALPs, it is the  $e^+e^- \rightarrow \gamma\gamma$  process. At 75 GeV, the total Bhabha cross section within

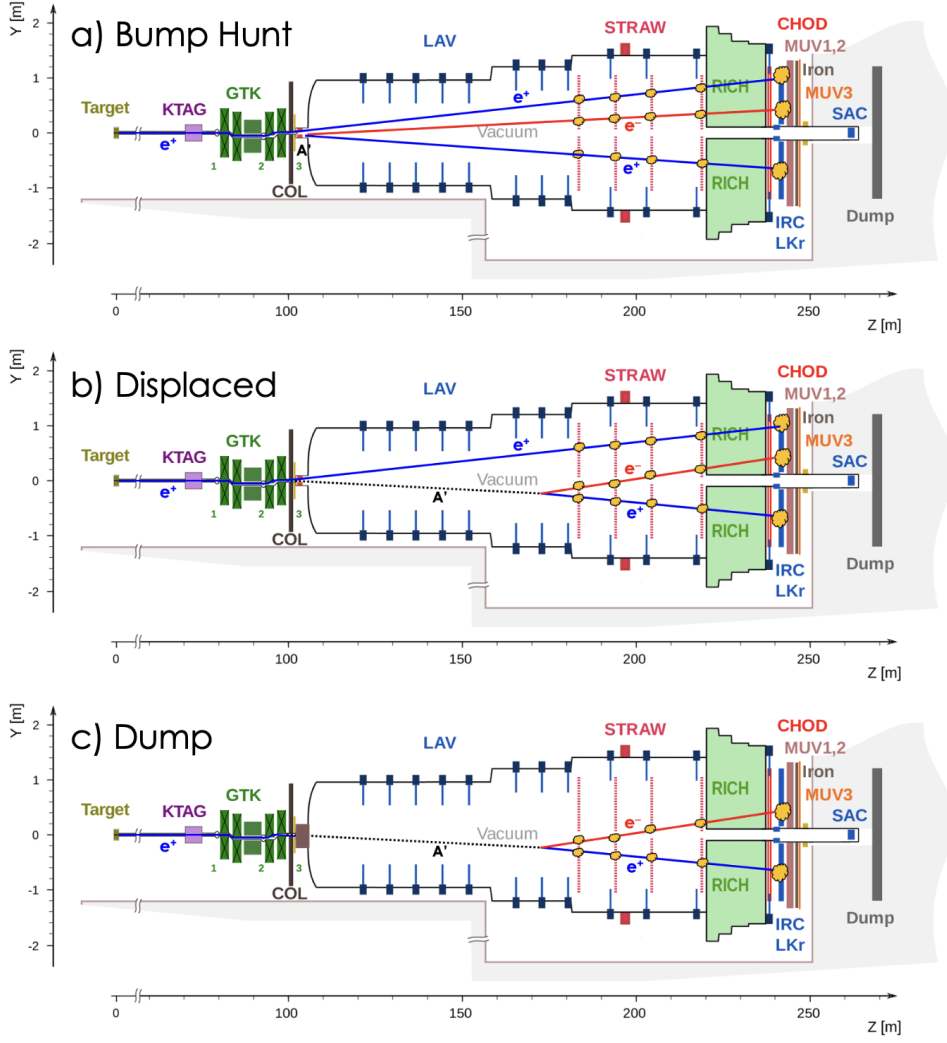


Figure 15: NA62e<sup>+</sup>'s visible decay search techniques. a) Bump hunt b) Displaced vertex c) Dump mode.

the NA62e<sup>+</sup> angular acceptance is  $\sim 9 \times 10^6$  pb, while the cross section for  $e^+e^- \rightarrow \gamma\gamma$  is  $1.4 \times 10^6$  pb, posing significant challenges to visible decay searches.

Evaluating the reach for all visible final states necessitates a reliable assessment of the SM background. This will be addressed in future work, potentially utilizing the existing NA62 experiment Monte Carlo simulation to provide robust estimates.

### 6.2. Long-living particles searches

Long-lived particles are natural dark sectors candidates. Their weak couplings to SM particles inherently leads to extended lifetimes. NA62 is uniquely equipped to directly measure the decay vertex positions of long-lived particles. The experiment's 70-meter long decay region, coupled with the high Lorentz boost provided by the 75 GeV positron beam, creates an ideal environment for such searches. Two experimental strategies, illustrated in Fig. 15, can be employed to distinguish long-lived particles from SM background. The displaced vertex technique, panel b), involves measuring the decay vertex and focusing the search on events exhibiting significantly displaced vertices. This approach, excluding mis-measured SM events, offers a nearly background-free environment for sufficiently long lifetimes.

In situations where precise vertex reconstruction is challenging or unavailable, a high-Z material block can be employed as an absorber to eliminate SM background, panel c). Only long-lived particles that decay after traversing the absorber, will produce a detectable signal, effectively suppressing all SM background. However, this approach requires dedicated data collection within NA62e<sup>+</sup>.

### 6.2.1. Thin target: displaced vertex

NA62's multi track vertex reconstruction capabilities have been demonstrated numerous times in kaon decay analyses, resulting in a decay vertex resolution of  $\sigma_{VTX} \sim 0.5$  m.

The displaced vertex technique, illustrated in Fig. 15 b), involves detecting di-lepton or di photon decays with a vertex located several meters away from the target. After complete energy reconstruction, the only remaining background consists of bremsstrahlung photon conversions, which can only occur outside the decay region which is maintained in high vacuum.

This technique can be applied across a variety of dark sector scenarios. In this section, we focus on DPs and ALPs. As demonstrated in thin target invisible searches, a leading sensitivity in DP case translates into a leading sensitivity in the ALPs with electron coupling. Models with ALPs featuring pure photon coupling are expected to demonstrate significantly higher sensitivity due to their extended lifetime,  $\tau = 64\pi/(m_a^3 g_{a\gamma}^2)$ , which enhances the experimental advantage of having a 70 m long decay region.

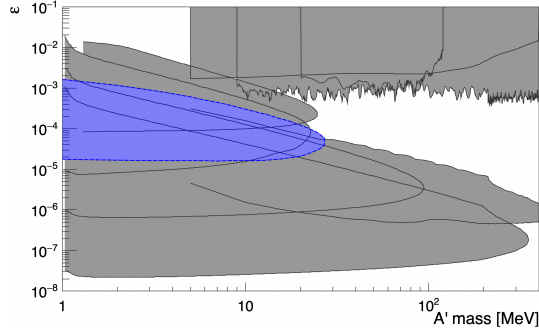


Figure 16: NA62e+  $A'$  displaced vertex sensitivity (Blue) compared to existing limits shown in grey. Dump experiments NA64 [45], E141 [46], KEK and Orsay [47, 48] KLOE [49], NA62 [15], bump hunt experiments KLOE [49], BaBar [38], NA48/2 [50]

In the DP case we conservatively calculate the number of  $A'$  produced in  $A'$ [VK: -strahlung] only. Measuring the recoil positron momentum will allow additional constraints reducing background. After determining the decay length starting from the  $A'$  width  $\Gamma$ , we estimate the probability of decay within the NA62 decay region as:

$$P(L_{min}, L_{max}) = e^{-\frac{L_{min}}{L_{dec}}} - e^{-\frac{L_{max}}{L_{dec}}} \quad (15)$$

The value of  $L_{min}$  depends solely on the NA62 vertex reconstruction capability and can be set at approximately  $5 \times \sigma_{VTX}$ . On the other end  $L_{max}$  is limited by the distance between the target and the first spectrometer station, around 70 m.

With  $2 \times 10^{14}$  75 GeV  $e^+oT$  and a decay region defined by  $L_{min} = 2.5$  m and  $L_{max} = 70$  m, the parameter space accessible for  $A'$  displaced vertex searches has already been explored by previous dump experiments (see Fig. 16). Competitive results for  $A'$  displaced vertex searches in thin target mode require  $2 \times 10^{15}$   $e^+oT$ . Under these conditions, managing detector and trigger rates, as well as mitigating SM background, would pose significant challenges.

### 6.2.2. Thick target: dump mode

An alternative approach to leveraging the particle's lifetime is to use an absorber (dump) to suppress prompt Standard Model (SM) background. The NA62 experiment has previously demonstrated successful operation in dump mode [15]. Compared to the  $\sim 5 \times 10^{17}$  proton on dump collected by NA62, the flux of positrons will be significantly lower, not exceeding approximately  $10^{15}$  positrons on target. Nevertheless, the yield of dark sector particles is higher when positrons are used, due to  $X$ -strahlung. In addition, in proton dump mode the production is dominated by mesons decays reducing the momentum of dark sector particles and their decay length.

As demonstrated by the NA64 experiment, an absorber  $\lesssim 50$  cm thick is sufficient to contain a positron beam of energy  $\gtrsim 100$  GeV. Dumping the positron beam at the beginning of the NA62 decay region will allow NA62e+ to obtain high acceptance with a positron flux potentially 1000 times higher with respect to NA64 [45, 51].

In Fig. 17, the blue filled area represents the expected NA62e+ sensitivity for  $2 \times 10^{14}$   $e^+OT$  impinging on a tungsten dump with a thickness of  $d_{th} = 35$  cm ( $100 X_0$ ). Decays of long lived meson

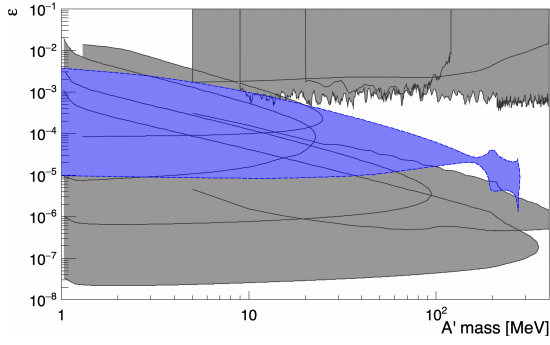


Figure 17: NA62e+  $A'$  sensitivity with  $2 \times 10^{14}$   $e^+oT$  and  $d_{th}=35$  cm (blue), compared to existing limits (gray).

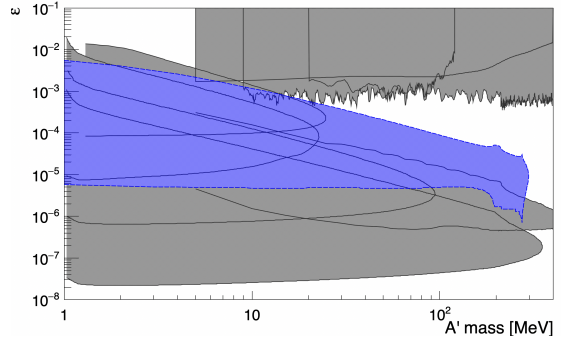


Figure 18: NA62e+  $A'$  sensitivity with  $2 \times 10^{15}$   $e^+oT$  and  $d_{th}=35$  cm (blue), compared to existing limits (gray).

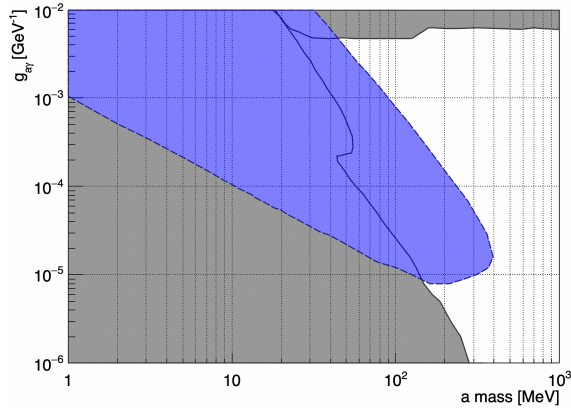


Figure 19: NA62e+ dump mode sensitivity to visible decays of ALPs with photon-dominant coupling (blue). In gray existing limits from LEP [53], NA64 [54], and dump experiments as in Fig.16

downstream the dump will be detected with extremely high efficiency by the NA62 apparatus. The gray filled region on the bottom indicates exclusions from beam dump experiments, while the region on the top corresponds to bump hunt exclusions from NA48/2 ( $\pi^0 \rightarrow \gamma A'$  [50]), BaBar ( $e^+e^- \rightarrow \gamma A'$  [52]), and KLOE [49]. Note that the  $A'$  production rates that we have been using include for the first time all the diagrams shown in Fig. 7 along with the electron motion effects described in [5] for the resonant process. Even with  $2 \times 10^{14}$   $e^+oT$ , the visible dump mode allows access to a large unexplored region of the DP parameter space.

As shown in Tab. 1, approximately  $10^{15}$  positrons on target per year can be produced in a BDF-like scenario at 75 GeV. However, radiation protection and safety concerns must be carefully assessed, as they could present significant challenges to implementing this technique within the TTC8 cavern.

In Fig. 18, the expected sensitivity for  $2 \times 10^{15}$   $e^+oT$  is illustrated. Under these conditions, the sensitivity is extended in the 100–200 MeV region, reaching the exclusion limit of the NA62 in dump mode [15]. Raising the energy to 150 GeV is not a viable strategy, as this would lead to approximately a tenfold reduction in the positron rate, as shown in Fig.4.

Using Primakoff production rates obtained from `MadGraph5_aMC@NLO`, with the requirement that the ALP carries more than 50% of the beam energy, we derived the NA62e+ sensitivity in dump mode to ALPs with photon coupling, as shown in Fig. 19, assuming zero background. In this scenario, NA62e+ can achieve world-leading limits in the 50–400 MeV region.

## 7. Non minimal dark sectors

In addition to the minimal portal scenario already described, more elaborate models can produce observable final states in NA62e+. Detailed investigations of additional dark sector cases were performed in [55] for the LDMX experiment, including dark photons, Axion-Like Particles, dark scalars, milli-charged particles, and B-L new gauge boson models.

While expected limits from NA62e+ are not computed here, they can be extrapolated from the plots in [55]. In general, limits from NA62e+ are expected to be stronger compared to electron beam ones for the same number of particles on target due to the additional contribution specific for positrons. This section will address extensions with an additional dark Higgs, which is not covered in [55].

Non-minimal extension of the Standard Model (SM) by adding a new  $U(1)_D$  gauge boson,  $A'$ , and a single complex scalar Higgs field,  $\phi$ , responsible for spontaneous symmetry breaking have been described in [56]. In the case were possible additional dark sector particles (such as a new dark matter candidate for instance) are heavy compared to the dark photon  $A'$  and dark Higgs  $h'$  mass scales, the phenomenology at accelerators is mainly driven by these two particles.

All interactions between the SM and the secluded sector occur through kinetic mixing of  $U(1)_D$  with the Standard Model photon. The dark Higgs (DH) decay channels depend on whether it is heavier or lighter than the dark photon  $A'$ . We will focus on the case  $m_{h'} > 2m_{A'}$ , in which the  $h'$  mainly decays to a pair of real dark photons. The decay is always prompt, since the lifetime only depends on the dark gauge coupling  $g_D$  which is supposed to be of order one. For c.m. energies below  $\sim 200$  MeV, the phenomenology is simpler than that described in [56]. Indeed, neglecting the possible decay to neutrinos, which is extremely suppressed at this energy, the only possible  $A'$  decay is in  $e^+e^-$  pairs. The  $h'$ -strahlung process is one of the few tree level production mechanisms for  $h'$ . The amplitude is suppressed by only a single power of the kinetic mixing constant, making  $h'$  production feasible to occur in the range of  $\epsilon \mathcal{O}(10^{-2} - 10^{-3})$ . The complete decay chain of interest in NA62e+ is shown in Fig. 20.

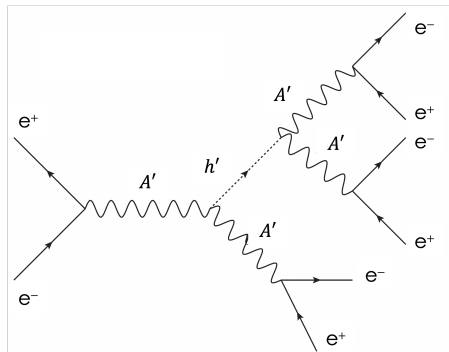


Figure 20: The 6 leptons process  $e^+e^- \rightarrow 3e^+e^-$  mediated by Dark Higgs.

The total cross section for the Higgs'-strahlung process,  $e^+e^- \rightarrow [VK : A']h'$ , shown in Fig. 20, is [56]:

$$\sigma_{e^+e^- \rightarrow A'h'} = \frac{\pi\alpha\alpha_D\epsilon^2}{3s} \left(1 - \frac{m_{A'}^2}{s}\right)^{-2} \sqrt{\lambda\left(1, \frac{m_{h'}^2}{s}, \frac{m_{A'}^2}{s}\right)} \left[ \lambda\left(1, \frac{m_{h'}^2}{s}, \frac{m_{A'}^2}{s}\right) + \frac{12m_{A'}^2}{s} \right] \quad (16)$$

Using  $m_{A'} = 10$  MeV,  $m_{h'} = 50$  MeV,  $\alpha_D = 1$ , and  $\epsilon = 1 \times 10^{-3}$  we obtain a total cross section of approximately 3.7 pbarn. The main Standard Model background process,  $e^+e^- \rightarrow 6e^\pm$ , is significantly suppressed due to its proportionality to  $\alpha^6$ . A recent revision of the Equivalent Photon Approximation calculations has led to the following expression for the cross section [57]:

$$\sigma_{ee \rightarrow 6e} = \frac{\alpha^2}{6\pi^2} \sigma_{(\gamma\gamma \rightarrow 2e^+e^-)} \left( \log^4\left(\frac{s}{m^2}\right) + A \log^3\left(\frac{s}{m^2}\right) + B \log^2\left(\frac{s}{m^2}\right) + C \log\left(\frac{s}{m^2}\right) + D \right) \quad (17)$$

where the constant coefficients have the following values:

$$A \sim -11.9 \quad B \sim 22.62 \quad C \sim 143.5 \quad D \sim -521.1 \quad (18)$$

At 75 GeV positron beam energy the SM  $6e$  background cross section value is  $0.04 \mu\text{barn}$ . Given the constraints of having each of the pair of lepton sharing the same invariant mass, namely the  $A'$  mass, the background can be suppressed by several orders of magnitude as demonstrated by Babar [58] and Belle [59] studies. We expect the DH to six leptons searches at NA62e+ to have no background. The strongest constraints on this models coming from Belle experiment [59] are shown in Fig. 21. The Belle search covered the region of  $0.1 < m_{A'}/\text{GeV} < 3.5$  and  $0.2 < m_{h'}/\text{GeV} < 10.5$ , respectively. In the mass region  $m_{h'} < 200$  MeV NA62 should be able to provide the most stringent constraints. In zero background hypothesis, the NA62e+ experiment could potentially

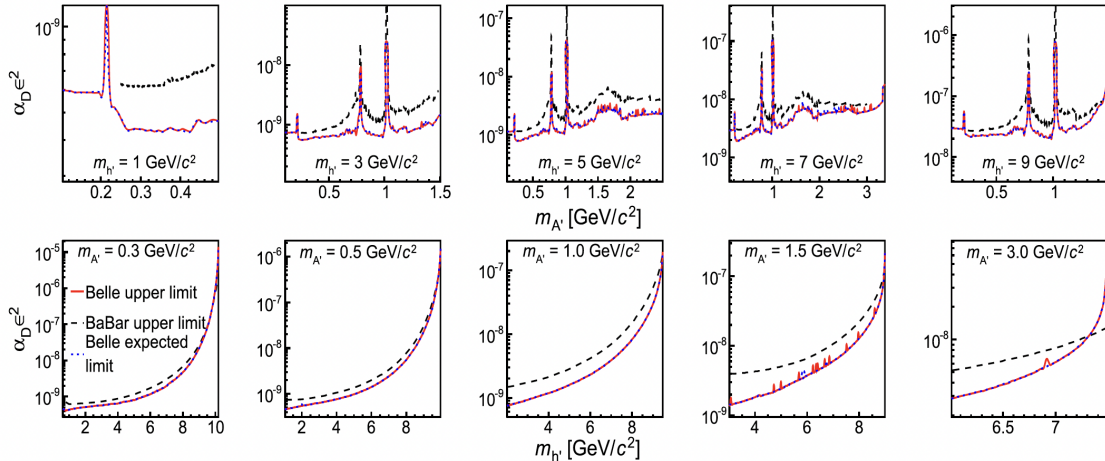


Figure 21: 90% C.L. upper limit on the product  $\alpha_D \epsilon^2$  versus dark photon mass (top row) and dark Higgs boson mass (bottom row) for Belle (solid red curve) and BABAR (dashed black curve) [59].

achieve limits on  $\epsilon \alpha_D$  as low as  $\sim 10^{-8}$ , profiting from the cross section enhancement due to the lower c.m. energy compared to B-factories. However, more detailed studies on detector acceptance and actual sensitivity are beyond the scope of this paper.

## 8. Standard model physics

Standard model cross sections for  $e^+e^-$  collisions are per se an important part of the physics case. The NA62e+ luminosity at a c.m. energy below 300 MeV is unprecedented and can provide precise measurement of standard model observables in an almost unexplored regime.

### 8.1. Mesons photo-production and invisible mesons decays

A recent study [44] has demonstrated that electron-on-target dark sector experiments are able to produce a large amount of light mesons through exclusive forward photo-production. The mechanism requires a high energetic photon to be produced by SM bremsstrahlung in the interaction of the electron or positron with the experiment target. Subsequently, the photon undergoes an exclusive photo-production process producing a single light vector meson (V). Following the order of magnitude approximations in [44], the number of produced mesons ( $N_V$ ) can be obtained as:

$$N_V = N_e f_{brem} p_V \quad p_V \approx \frac{9 \sigma_0^V X_0 f_{nucl}^V}{7 m_p} \quad \sigma_{\gamma N \rightarrow V N} = f_{nucl}^V A \sigma_0^V \quad (19)$$

where  $\sigma_0^V$  is the cross section on a single nucleon  $\sim 1 \mu\text{b}$ , and  $f_{nucl}^V$  is an order 1 correction factor. If any of these mesons decay invisibly, it will produce a missing energy/momentum signal detectable by NA64 or LDMX [44]. This allows us to translate missing energy/momentum limits into constraints on  $BR(\rho, \omega, \phi, J/\psi) \rightarrow \text{Invisible}$ .

In Tab. 4, we updated the NA64 meson yields based on Ref. [2] and estimated those for NA62e+ in thick target mode by scaling the NA64 values (see Table II in [44]). The meson yields exceed  $10^8$ , except for  $J/\Psi$ . A null result in the missing energy experiment would translate into  $\sim 10^{-8}$  limits on meson invisible decays, which is more than 1000 times stronger than current bounds (see Table 1 in Ref. [44]).

In the thin target mode,  $\approx 15\%$  of this yield is produced by the  $500 \mu\text{m}$  W target resulting in  $\approx 4 \times 10^7$  mesons, still producing very stringent bounds. In addition, in thin target mode the

|         | $N_{e+OT}$         | $E_e$ | $f_{\text{brem}}$ | $\sigma_0^\rho$ ( $\mu\text{b}$ ) | $\sigma_0^\omega$ ( $\mu\text{b}$ ) | $\sigma_0^\phi$ ( $\mu\text{b}$ ) | $N_\rho$          | $N_\omega$        | $N_\phi$          | $N_{J/\psi}$    |
|---------|--------------------|-------|-------------------|-----------------------------------|-------------------------------------|-----------------------------------|-------------------|-------------------|-------------------|-----------------|
| NA64[2] | $1 \times 10^{12}$ | 100   | 0.5               | 9                                 | 0.8                                 | 0.7                               | $2.5 \times 10^7$ | $2 \times 10^6$   | $2 \times 10^6$   | $2 \times 10^4$ |
| LDMX I  | $4 \times 10^{14}$ | 4     | 0.03              | 23                                | 5                                   | 0.4                               | $1.1 \times 10^9$ | $1.9 \times 10^8$ | $1.1 \times 10^7$ | –               |
| NA62e+  | $2 \times 10^{14}$ | 75    | 0.5               | 9                                 | 0.8                                 | 0.7                               | $5 \times 10^9$   | $4 \times 10^8$   | $4 \times 10^8$   | $4 \times 10^6$ |

Table 4: Estimated meson yield from Tab. II in [44]. We updated NA64 yield according to [2] and added an estimate for NA62e+ thick target mode.

energy of the photon that produced the meson can be derived measuring the momentum of the recoil positron. Tagging the mesons by their decay products and invariant mass, a measurement of the photo-production cross section as a function of the photon energy can be derived with high precision. Future proton beam dumps such as SHiP will benefit a lot from this kind of measurements since, in their case, meson decays are an important source of DM. Typically, proton beam dump Monte Carlo simulations are tuned to match data but they just reach  $\sim 25\%$  level agreement [60].

### 8.2. The $e^+e^- \rightarrow \pi\pi$ cross section

The  $(g-2)_\mu$  anomaly is one of the most significant and longstanding discrepancies between an experimental measurement and the Standard Model. Following the confirmation of earlier experimental results by E821 [61] obtained by the Muon  $g-2$  Experiment at Fermilab [62], attention has increasingly turned to the theoretical predictions. These are carried out from first principles, by means of QCD lattice techniques, or via a data driven approach that uses as input the hadronic cross section. For this reason the measurement of the hadronic cross section at low energies is of great importance for the improvement of the theoretical error, and a particularly important role in this context is played by the dominant hadronic production process  $e^+e^- \rightarrow \pi^+\pi^-$ .

Currently, the most precise determinations of  $e^+e^- \rightarrow \pi\pi$  as a function of  $\sqrt{s}$  rely on the initial-state radiation technique, a method used e.g. by KLOE [63] and BaBar [64, 65]. Unfortunately, their results exhibit a  $\sim 3\sigma$  discrepancy.<sup>2</sup> The hadronic cross section as a function of the c.m. energy can be also measured by varying directly the energy of the electron and positron beams, a technique that has been used for the CMD-3 measurement. It is worrisome that the latest CMD-3 result [68] is not consistent with neither the one of KLOE nor BaBar.

Recently, Ref. [6] proposed to leverage the momentum distribution of atomic electrons in positron annihilation on the electrons of a fixed target to scan over a large range of c.m. energies, while keeping the beam energy fixed. A proper high  $Z$  material target can allow precise measurements of hadronic cross sections in a wide  $\sqrt{s}$  region. It was shown in Ref. [6] that with  $10^{16}$   $e^+oT$  a CERN north area experiment could yield a statistic larger than KLOE up to c.m. energies of  $\sim 600$  MeV.

With a modest increase in the bending power of the achromats, NA62e+ could surpass the di-pion production threshold at a beam energy of 88 GeV. Utilizing a few  $10^{14}$  positrons on target could achieve the statistical sensitivity required for a precise measurement of the di-pion cross-section near threshold, unlike previous measurements by KLOE and BaBar. By avoiding the reliance on ISR-based techniques, the NA62e+ measurement would be less affected by theoretical uncertainties, offering a robust and precise determination of this key cross-section. While detailed studies of this opportunity are outside the scope of this paper, we point out that the PID system of NA62 will allow for excellent lepton-hadron separation leading to very precise measurements at threshold.

### 8.3. Study of the di-muon production cross section

A measurement of the  $e^+e^- \rightarrow \mu^+\mu^-$  cross section with per-mille precision can be achieved during a one-year run in positron mode at NA62e+. The theoretical uncertainties for the  $e^+e^- \rightarrow \mu^+\mu^-$  cross section are estimated at the 0.2% level [69], demonstrating the significance of achieving such high precision. This measurement would provide valuable validation of QED in the low-energy region,  $\sqrt{s} \sim O(200)$  MeV, where no experimental data currently exists. In particular the observation of muon pair production with a beam energy below the threshold of 43.7 GeV for di-muon production off electrons-at-rest, will demonstrate unambiguously the effects of atomic electron motion and provide a validation in high energy collisions of theoretical predictions [6].

<sup>2</sup>The KLOE and BaBar determinations rely on the assumption that the scattering cross section for  $e^+e^- \rightarrow \mu^-\mu^-$  is determined solely by SM processes, see [66, 67] for a counterexample.



Finally, there is increasing interest in studying differential cross sections near the threshold, motivated by the proposed muon collider LEMMA scheme [7]. In particular the beam emittance and the di-muon yield as function of the target material obtained in simulations need to be validated. First test with low statistical significance have been performed in the past using H4 positron beams [70].

The production cross section decreases at the production threshold of 45 GeV, see Fig. 22, therefore 75 GeV is an excellent compromise.<sup>3</sup> The di-muon differential cross-section in the c.m. frame is equal to [71]:

$$\frac{d\sigma}{d\Omega} = \frac{\alpha^2}{4s} \beta S(\beta) (2 - \beta^2 \sin^2 \theta), \quad S(\beta) = \frac{X(\beta)}{1 - \exp(-X(\beta))}, \quad X(\beta) = \frac{\pi\alpha}{\beta} \sqrt{1 - \beta^2} \quad (20)$$

where  $\beta = \sqrt{1 - \frac{4m_\mu^2}{s}}$  and  $S(\beta)$  is the Sommerfeld-Schwinger-Sakharov threshold enhancement factor from Coulomb rescattering [72]. The total cross-section is found by integrating the differential formula:

$$\sigma = \frac{2\pi\alpha^2 \beta S(\beta)}{s} \left(1 - \frac{\beta^2}{3}\right) \quad (21)$$

and its dependence on the positron beam energy is represented in Figure 22.

At 75 GeV, the cross-section for the process  $\sigma_{e^+e^- \rightarrow \mu^+\mu^-}$  is 1.1,  $\mu\text{b}$ , which is very close to its maximum value. The maximum angle of the muons in the lab frame is approximately 3 mrad. Consequently, the acceptance is primarily limited by the lower bound of 0.73 mrad, determined by the inner hole (6 cm radius) of the straw tracker located 82 m downstream of the target. The angular distribution  $\theta_{lab}$  for the muon pair is shown in Figure 22, along with the straw tracker's blind region.

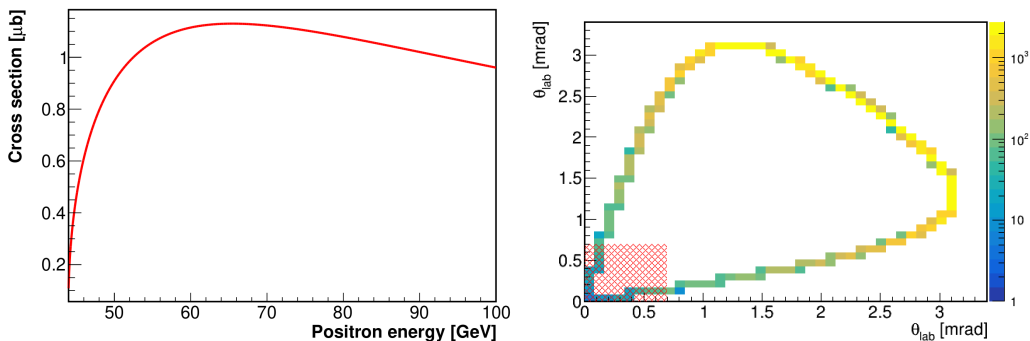


Figure 22:  $e^+e^- \rightarrow \mu^+\mu^-$  annihilation cross-section at fixed target, as a function of the positron beam energy (left) and distribution of  $\theta_{lab}$  for the two muons (right), with the straw tracker blind region in red .

The acceptance for  $\theta_{lab} > 0.73$  mrad, calculated by integrating the differential cross-section is approximately 86%. Assuming a  $\sim 80\%$  selection and reconstruction efficiency, and including the  $Z$  factor due to the target material,  $3.02 \times 10^{-8}$  events/ $e^+oT$  are expected for the 0.5 mm Si target and 5 times more in the W case.

In one year of data collection with a 75 GeV beam and a positron flux of  $2 \times 10^{14}$   $e^+oT$ , approximately  $N_{e^+e^- \rightarrow \mu^+\mu^-} \sim 6 \times 10^6$  events are expected, leading to a statistical uncertainty on the CS of  $\sim 0.05\%$ . The background contribution from misidentified Bhabha scattering events, is strongly suppressed by the NA62 PID system, while contributions from bremsstrahlung photon conversion in the field of a nucleus ( $\gamma N \rightarrow N\mu^+\mu^-$ ) and virtual photon bremsstrahlung from  $e^+$  scattering off a  $Z$  nucleus ( $e^+Z \rightarrow e^+Z\gamma^* \rightarrow e^+Z\mu^+\mu^-$ ) are suppressed by charged particle vetos and di-muon mass reconstruction. With proper control of systematic uncertainties, a few per-mille level precision in the measurement of the cross-section is achievable in short time scale.

<sup>3</sup>Notice that with enough statistics one could produce di-muons below the 45 GeV threshold by taking advantage of the tail of the atomic electron momentum distribution [6].

## 9. True muonium observation at NA62

Quantum electrodynamics (QED) predicts the existence of several bound states beyond standard atoms, including purely leptonic systems. The lightest such system, positronium ( $e^+e^-$ ), was discovered decades ago and has been extensively studied. True muonium (TM) ( $\mu^+\mu^-$ ) and true tauonium ( $\tau^+\tau^-$ ), however, have never been observed. This is primarily due to the lack of  $e^+e^-$  colliders operating at the appropriate c.m. energy to exploit the enhanced resonant cross-section, as well as challenges related to dissociation effects in matter that complicate fixed-target production. Atomic spectroscopy of true muonium is sensitive to contributions from hadronic vacuum polarization, such as those affecting the muon anomalous magnetic moment [73], as well as to potential new physics involving lepton couplings [74]. Before pursuing TM spectroscopy, an initial observation of true muonium is necessary to enable preliminary studies, validate production and decay models, and lay the groundwork for future investigations.

Many pathways for its discovery are known, but one of the most promising is resonant production using a positron beam impinging on multiple thin lithium targets [8], which is also doable at NA62. A dedicated low energy data taking period at the di-muon threshold (43.7 GeV) could be performed as positron yield per proton on target is expected to be higher with respect to the nominal 75 GeV as shown in Fig. 4. Together with possible true muonium discovery, the run will provide enhanced sensitivity to visible decays of low mass dark sectors candidates and useful information on the  $e^+e^- \rightarrow \mu^+\mu^-$  cross section production at threshold.

True muonium has two spin states: para-TM (spin 0), which decays into  $\gamma\gamma$ , and ortho-TM (spin 1), which decays into  $e^+e^-$ . The ortho-TM state can be observed at NA62 by searching for its displaced decay vertices in  $e^+e^-$ .

The probability of producing the ground state (1S) in  $e^+e^-$  interactions is  $\epsilon_{1S} = 83\%$ , and its lifetime at rest is 1.8 ps. This corresponds to a decay length of 11.3 cm for resonant production in a fixed-target setup [8]. Higher excited states ( $nS$ ) can also be produced, with probabilities  $\epsilon_{nS}$  proportional to  $n^{-3}$ , which slightly increase the signal yield. The impact of these higher excited states, which also have higher ( $\propto n^3$ ) lifetimes, and the potential for modifying the experimental setup to better exploit their production should be addressed in future studies, as these considerations are beyond the scope of this paper.

To compute true muonium production rate under realistic conditions, which involve non-negligible fluctuations in  $\sqrt{s}$  and initial state radiation effects [8], the peak  $e^+e^- \rightarrow TM$  cross-section  $\sigma_{peak}^{TM}$  of 66.6 nb must be scaled down by considering the probability  $p = 4.35 \times 10^{-4}$  that the beam c.m. energy falls within the energy window where bound states are allowed [72]. This window has a width equal to the TM binding energy of 1.4 keV. The effects of electron motion within the lithium target atoms and positron energy losses have also been included in the analysis [8]. However, their estimated impact is negligible given the NA62e+ beam energy spread of approximately 1%.

The most significant effect caused by matter is dissociation, as TM predominantly dissociates into  $\mu^+$  and  $\mu^-$  when passing through thick targets, with a dissociation cross-section of  $\sigma_d \sim 13Z^2$  b [75]. For lithium, the dissociation length is  $\mu_d^{-1} = 1.86$  mm. A practical approach is to use an assembly of multiple lithium targets, each 4 mm thick ( $\sim 2\mu_d^{-1}$ ), operated in vacuum. These targets should be spaced along the beam direction such that the majority of TM decays occur in the gaps between the targets.

The number of surviving TM atoms produced for one target per positron is [8]:

$$\frac{dTM}{de^+dN_{\text{target}}} = \frac{p\sigma_{peak}^{TM}}{13Z\text{ b}}(1 - e^{-\Delta z\mu_d})\epsilon_{nS} = 6.6 \times 10^{-13}\epsilon_{nS} \quad (22)$$

With a TM 1S decay length of 11.3 cm, a possible choice is to use 4 target cells, each featuring 4 berillium foils spaced by 20 cm with tracking stations between them., i.e. 2 silicon detectors with a 20 cm spacing, for a total of 8 silicon detectors and 20 lithium foils (see Fig. 23). Including a 10 cm spacing between the last silicon detector of a cell and the first of the next cell, every cell is 110 cm long, for a total length of the target-trackers system of 4.4 m.

### 9.1. Backgrounds discussion and detectors requirements

The  $e^+e^- \rightarrow e^+e^-$  Bhabha scattering represents the main source of background, as follows by the comparison of cross-section and the fact that it has the same c.m. energy and final states of TM  $e^+e^-$  decays [8]. Note that background coming from di-muon production can be safely

neglected due to the excellent particle identification capabilities of the NA62 experiment. From the experimental point of view, the only differences between Bhabha scattering process and TM production and decay in  $e^+e^-$  are the angular distribution in the c.m. frame and the non-zero decay length of TM.

An angular cut in the c.m.  $\frac{\pi}{4} < \theta_{cm} < \frac{3}{4}\pi$  was chosen, resulting in a decrease of signal yield of a factor  $\epsilon_{\theta_{cm}} = 62\%$  and a Bhabha cross-section of  $\sigma_{Bh.} = 21Z\mu b$ . The minimum (maximum) angle in the lab frame of the  $e^+/e^-$  originating from TM decays or Bhabha scattering are then 2.7 (16.6) mrad, corresponding to maximum (minimum) energies of 37.3 (6.4) GeV [8]. The NA62 straw tracker and LKr calorimeter are readily employable for this measurement. They are placed in a telescopic setup, meaning they have the same angular acceptance. The straw tracker has a hole at the center with a radius of 6 cm and an outer radius of 105 cm, with a distance between the first and last straw layer of 35 m [12]. By placing the first target at a distance of 28 m from the first straw layer, the acceptance for TM decay products with the above described  $\theta_{cm}$  cut is nearly 100%, as shown in figure 23. The only additional detectors required for the current NA62 setup

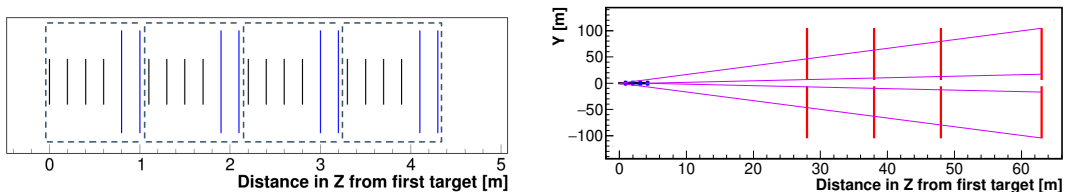


Figure 23: (left) Layout of the target-tracker setup: 4 cells with 4 lithium foils (black) and 2 silicon detectors (blue) each. (right) Layout of the targets together with the straw tube tracker modules (red) [12]. A distance of 28 m between the first target and the first tracker layer is chosen. Lines corresponding to minimum and maximum angles are drawn, respectively, in violet and green.

are the silicon detectors inside the target. Per-layer resolution of  $5\mu m$  and a material budget of  $0.3\%X_0$  are required, as estimated through simulations. Consequently, very thin monolithic pixel sensors, such as those planned for the ITS-3 ALICE upgrade or similar products [76], are necessary.

## 9.2. Monte Carlo Simulations

A simulation with  $10^{14} e^+oT$  was conducted to demonstrate the feasibility of efficiently suppressing the QED background by distinguishing true muonium (TM) decays with displaced vertices from Bhabha scattering originating in the targets [8].

A calorimeter resolution of  $\sigma_E/E = 5\%/\sqrt{E[\text{GeV}]} \oplus 10\%/E[\text{GeV}] \oplus 1\%$ , similar to that of the LKr calorimeter, was used. To identify Bhabha + TM events within the  $\theta_{cm}$  acceptance, a series of pre-selection cuts were applied. The vertex  $z$  of  $e^+e^-$  candidates was then reconstructed, followed by additional quality cuts, resulting in a total reconstruction efficiency of  $\epsilon_{reco} = 77.4\%$ . The identification of TM decays versus Bhabha scattering is achieved by applying cuts on the reconstructed vertex in the  $z$ -direction (see Fig. 24), after all other cuts. Background-free regions in  $z$  are selected, so the expected background is determined by the simulated statistics, yielding  $10^{-14}$  BG events per  $e^+oT$  for one cell.

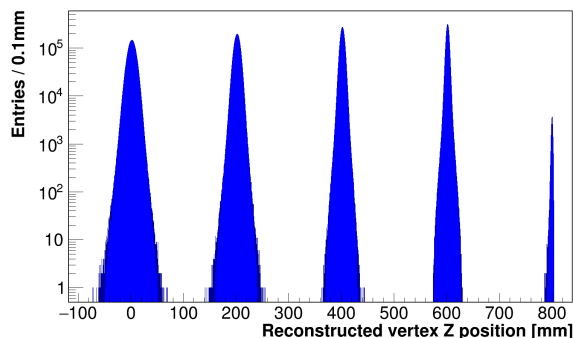


Figure 24: Reconstructed vertex  $z$  position after all other cuts for 4 targets of one simulated cell. The data at 800mm provide a very small yield and are due to fake vertices inside the first silicon detector.

The cuts on the vertex  $z$  position have different efficiency for TM events coming from different targets. The average value for these efficiencies is  $42.5\%$  [8].

### 9.3. Discovery potential

Depending on the experimental needs and data-taking time requirements for the primary goal of the experiment, which is dark sector searches, TM discovery could be conducted in either a short run (less than one month or even one week) using a dedicated target setup or a section of it, or in an approximately 3-month-long run using a less demanding setup with only one lithium target and two silicon tracker stations.

### 9.4. Dedicated target setup: 16 target stations

With the full target assembly discussed above, a discovery is possible in a very short time, making it the best choice in case of limited time at 43.6 GeV.

The global efficiency in equation (22) is evaluated by combining the probability to produce a 1S TM ( $\epsilon_{1S} = 83\%$ ), the angular efficiency ( $\epsilon_{\theta_{em}} = 62\%$ ), the reconstruction efficiency ( $\epsilon_{reco} = 77.4\%$ ), and the vertex-based selection efficiency ( $\epsilon_v = 42\%$ ), reaching a value of  $\epsilon_{tot} = 16.5\%$ . After multiplying by the number of targets ( $N_{target} = 16$ ), the value of selected TM per  $e^+oT$  is evaluated to be:

$$\frac{N_{TM}}{e^+oT} = \epsilon_{tot} N_{target} \cdot 6.6 \times 10^{-13} = 1.74 \times 10^{-12} \quad (23)$$

The expected background yield per  $e^+oT$ , given the simulated statistics of ( $10^{14}$   $e^+oT$ ) per cell and on the number of cells  $N_{cells} = 4$  is:

$$\frac{N_{BG}}{e^+oT} = \frac{N_{cells}}{10^{14}} = 4 \times 10^{-14} \quad (24)$$

corresponding to a S/BG ratio of roughly 20.

In a data-taking period of 1 month out of 7 total months/year of data-taking,  $e^+oT = 2 \times 10^{14}/7 = 2.8 \times 10^{13}$ , therefore 48.8(1.1) signal (background) events are expected, corresponding to an  $16.8\sigma$  significance, which motivates hopes for a discovery also when including all experimental effects neglected in the toy simulation. Moreover, a discovery level of significance of  $6.7\sigma$  could also be reached in a very short dedicated run of just one week.

### 9.5. Parasitic setup with single target station

In order to reduce costs and the impact of the target installation on the main experiment schedule, a simplified target station can be used in parasitic mode.

In this case, only the last target of the assembly sketched above would be used, therefore  $\epsilon_v = 56\%$  (see Table II of [8]), translating in  $1.45 \times 10^{-13}$  TM/ $e^+oT$  and  $2.5 \times 10^{-15}$  BGK/ $e^+oT$  events. In a period of 3 months out of 7 total months/year of SPS standard data-taking,  $e^+oT = 2 \times 10^{14} \times 2/7 = 5.7 \times 10^{13}$ , therefore 8.3(0.14) signal (background) events are expected, corresponding to an  $7.2\sigma$  significance.

## 10. Conclusions

In this paper, we propose a potential physics program for ECN3, utilizing the existing NA62 detector and a newly developed high-intensity 75 GeV positron beam. By capitalizing on the high proton flux expected following the post-LS3 upgrades in the North Area, we suggest that positron fluxes  $\sim 2 \times 10^{14} e^+ oT$  per year can be achieved with minor modifications to the NA beam line setup.

A dedicated feasibility and performance study by the CERN accelerator division on the development of a high-energy positron beam line in ECN3 would be highly desirable. Such a study would help determine the maximum achievable positron beam flux under various future North Area scenarios. While this paper does not evaluate hadron contamination in the beam or propose mitigation strategies, these aspects are critical for a more comprehensive assessment of the experiment’s potential for dark sector searches. The design of the T4 wobbling station, radio protection constraints, and the increased proton flux foreseen for the NA upgrades, make the ECN3 cavern the optimal location to achieve and effectively utilize the highest positron flux. Furthermore, the extended decay region, wide angular coverage of the veto systems, and the high-performance particle identification capabilities of the NA62 detector provide substantial advantages in suppressing background.

The proposed physics program focuses on dark sector searches using positrons on thin target collisions and positron dump mode. We have demonstrated that the NA62e+ experiment can achieve leading sensitivity to both visible and invisible decays of dark photons and ALPs within a short time frame. The program can also include critical precision tests of the Standard Model, conducted concurrently with the thin target experiments. Precise measurements of hadronic cross-sections at low  $\sqrt{s}$  can provide significant insights into the  $(g-2)_\mu$  anomaly, contributing to a deeper understanding of this long-standing discrepancy.

Moreover, by reducing the c.m. energy to the di-muon production threshold ( $E_{\text{Beam}} \sim 45$  GeV),  $e^+e^- \rightarrow \mu^+\mu^-$  interactions can be precisely studied, including the potential for the first observation of true muonium atoms.

Finally, the physics program can be expanded to encompass additional dark sector models, such as inelastic dark matter, millicharged particles, and  $B - L$  scenarios. The NA62e+ program will have the unique capability to probe the background limits of nearly all dark sector search techniques utilizing positrons on target, laying the foundation for future investigations at the extracted beam lines of the FCC-ee accelerator.

## Acknowledgments

The work of M.R. was partially supported by CERN scientific associate program. F.A.A., G.G.d.C. and E.N. are supported in part by the INFN “Iniziativa Specifica” Theoretical Astroparticle Physics (TAsP). F.A.A. received additional support from an INFN Cabibbo Fellowship, call 2022. The work of E.N. is supported by the Estonian Research Council, grant PRG1884. Partial support from the CoE grant TK202 “Foundations of the Universe”, from the CERN and ESA Science Consortium of Estonia, grants RVTT3 and RVTT7, and from the COST (European Cooperation in Science and Technology) Action COSMIC WISPerS CA21106 is also acknowledged.

## References

- [1] T. Åkesson, et al., [Dark Sector Physics with a Primary Electron Beam Facility at CERN](#), Tech. rep., CERN, Geneva (2018).  
URL <https://cds.cern.ch/record/2640784>
- [2] Y. M. Andreev, et al., Search for Light Dark Matter with NA64 at CERN, *Phys. Rev. Lett.* 131 (16) (2023) 161801. [arXiv:2307.02404](#), [doi:10.1103/PhysRevLett.131.161801](#).
- [3] Y. M. Andreev, et al., Measurement of the intrinsic hadronic contamination in the NA64—e high-purity  $e^+/e^-$  beam at CERN, *Nucl. Instrum. Meth. A* 1057 (2023) 168776. [arXiv:2305.19411](#), [doi:10.1016/j.nima.2023.168776](#).
- [4] E. Nardi, C. D. R. Carvajal, A. Ghoshal, D. Meloni, M. Raggi, Resonant production of dark photons in positron beam dump experiments, *Phys. Rev. D* 97 (9) (2018) 095004. [arXiv:1802.04756](#), [doi:10.1103/PhysRevD.97.095004](#).

- [5] F. Arias-Aragón, L. Darmé, G. G. di Cortona, E. Nardi, Production of Dark Sector Particles via Resonant Positron Annihilation on Atomic Electrons, *Phys. Rev. Lett.* 132 (26) (2024) 261801. [arXiv:2403.15387](#), [doi:10.1103/PhysRevLett.132.261801](#).
- [6] F. Arias-Aragón, L. Darmé, G. Grilli di Cortona, E. Nardi, *Atoms as electron accelerators for measuring the cross section of  $e^+e^- \rightarrow$  Hadrons*, *Phys. Rev. Lett.* 134 (2025) 061802. [doi:10.1103/PhysRevLett.134.061802](#).  
URL <https://link.aps.org/doi/10.1103/PhysRevLett.134.061802>
- [7] M. Antonelli, M. Boscolo, R. Di Nardo, P. Raimondi, Novel proposal for a low emittance muon beam using positron beam on target, *Nucl. Instrum. Meth. A* 807 (2016) 101–107. [arXiv:1509.04454](#), [doi:10.1016/j.nima.2015.10.097](#).
- [8] R. Gargiulo, S. Palmisano, E. Di Meo, *Feasibility study of true muonium discovery with the cern-sps h4 positron beam*, *Phys. Rev. D* 110 (2024) 092015. [doi:10.1103/PhysRevD.110.092015](#).  
URL <https://link.aps.org/doi/10.1103/PhysRevD.110.092015>
- [9] C. Ahdida, et al., Post-LS3 Experimental Options in ECN3 (10 2023). [arXiv:2310.17726](#).
- [10] D. Banerjee, J. Bernhard, M. Brugger, N. Charitonidis, N. Doble, L. Gatignon, A. Gerbershagen, *The North Experimental Area at the Cern Super Proton Synchrotron* Dedicated to Giorgio Brianti on the 50th anniversary of his founding the SPS Experimental Areas Group of CERN-Lab II and hence initiating the present Enterprise. (2021). [doi:10.17181/CERN.GP3K.OS1Y](#).  
URL <https://cds.cern.ch/record/2774716>
- [11] M. U. Ashraf, et al., High Intensity Kaon Experiments (HIKE) at the CERN SPS Proposal for Phases 1 and 2 (11 2023). [arXiv:2311.08231](#).
- [12] E. Cortina Gil, et al., The Beam and detector of the NA62 experiment at CERN, *JINST* 12 (05) (2017) P05025. [arXiv:1703.08501](#), [doi:10.1088/1748-0221/12/05/P05025](#).
- [13] E. Cortina Gil, et al., Search for a feebly interacting particle  $X$  in the decay  $K^+ \rightarrow \pi^+ X$ , *JHEP* 03 (2021) 058. [arXiv:2011.11329](#), [doi:10.1007/JHEP03\(2021\)058](#).
- [14] E. Cortina Gil, et al., Search for  $\pi^0$  decays to invisible particles, *JHEP* 02 (2021) 201. [arXiv:2010.07644](#), [doi:10.1007/JHEP02\(2021\)201](#).
- [15] E. Cortina Gil, et al., Search for Leptonic Decays of Dark Photons at NA62, *Phys. Rev. Lett.* 133 (11) (2024) 111802. [arXiv:2312.12055](#), [doi:10.1103/PhysRevLett.133.111802](#).
- [16] H. W. Atherton, P. Coet, N. T. Doble, D. E. Plane, *Electron and photon beams in the SPS experimental areas*, Tech. rep., CERN, Geneva (1985).  
URL <https://cds.cern.ch/record/164934>
- [17] G. Mazzola, L. S. Esposito, *P42 T4/XTAX transmission efficiency - FLUKA* (2023).  
URL <https://cds.cern.ch/record/2865692>
- [18] R. B. Appleby, J. Bernhard, J. B. Dainton, L. Gatignon, E. Goudzovski, G. A. Burton, R. Jones, C. Lazzeroni, A. Romano, G. Ruggiero, S. Tygier, *Considerations for a RF separated K+ beam for NA62* (2021).  
URL <https://cds.cern.ch/record/2765940>
- [19] G. Anzivino, et al., Construction and test of a RICH prototype for the NA62 experiment, *Nucl. Instrum. Meth. A* 593 (2008) 314–318. [doi:10.1016/j.nima.2008.05.029](#).
- [20] F. Hahn, F. Ambrosino, A. Ceccucci, H. Danielsson, N. Doble, F. Fantechi, A. Kluge, C. Lazzeroni, M. Lenti, G. Ruggiero, M. Sozzi, P. Valente, R. Wanke, *NA62: Technical Design Document*, Tech. rep., CERN, Geneva (2010).  
URL <https://cds.cern.ch/record/1404985>
- [21] T. Åkesson, et al., Light Dark Matter eXperiment (LDMX) (8 2018). [arXiv:1808.05219](#).
- [22] C. Antel, et al., Feebly-interacting particles: FIPs 2022 Workshop Report, *Eur. Phys. J. C* 83 (12) (2023) 1122. [arXiv:2305.01715](#), [doi:10.1140/epjc/s10052-023-12168-5](#).

- [23] Y.-S. Tsai, V. Whitis, THICK TARGET BREMSSTRAHLUNG AND TARGET CONSIDERATION FOR SECONDARY PARTICLE PRODUCTION BY ELECTRONS, *Phys. Rev.* 149 (1966) 1248–1257. [doi:10.1103/PhysRev.149.1248](https://doi.org/10.1103/PhysRev.149.1248).
- [24] L. Marsicano, M. Battaglieri, M. Bondi', C. D. R. Carvajal, A. Celentano, M. De Napoli, R. De Vita, E. Nardi, M. Raggi, P. Valente, Dark photon production through positron annihilation in beam-dump experiments, *Phys. Rev. D* 98 (1) (2018) 015031. [arXiv:1802.03794](https://arxiv.org/abs/1802.03794), [doi:10.1103/PhysRevD.98.015031](https://doi.org/10.1103/PhysRevD.98.015031).
- [25] Y.-S. Tsai, AXION BREMSSTRAHLUNG BY AN ELECTRON BEAM, *Phys. Rev. D* 34 (1986) 1326. [doi:10.1103/PhysRevD.34.1326](https://doi.org/10.1103/PhysRevD.34.1326).
- [26] J. D. Bjorken, R. Essig, P. Schuster, N. Toro, New Fixed-Target Experiments to Search for Dark Gauge Forces, *Phys. Rev. D* 80 (2009) 075018. [arXiv:0906.0580](https://arxiv.org/abs/0906.0580), [doi:10.1103/PhysRevD.80.075018](https://doi.org/10.1103/PhysRevD.80.075018).
- [27] A. Celentano, L. Darmé, L. Marsicano, E. Nardi, New production channels for light dark matter in hadronic showers, *Phys. Rev. D* 102 (7) (2020) 075026. [arXiv:2006.09419](https://arxiv.org/abs/2006.09419), [doi:10.1103/PhysRevD.102.075026](https://doi.org/10.1103/PhysRevD.102.075026).
- [28] J. Alwall, R. Frederix, S. Frixione, V. Hirschi, F. Maltoni, O. Mattelaer, H. S. Shao, T. Stelzer, P. Torrielli, M. Zaro, The automated computation of tree-level and next-to-leading order differential cross sections, and their matching to parton shower simulations, *JHEP* 07 (2014) 079. [arXiv:1405.0301](https://arxiv.org/abs/1405.0301), [doi:10.1007/JHEP07\(2014\)079](https://doi.org/10.1007/JHEP07(2014)079).
- [29] L. Darmé, F. Giacchino, E. Nardi, M. Raggi, Invisible decays of axion-like particles: constraints and prospects, *JHEP* 06 (2021) 009. [arXiv:2012.07894](https://arxiv.org/abs/2012.07894), [doi:10.1007/JHEP06\(2021\)009](https://doi.org/10.1007/JHEP06(2021)009).
- [30] Q. Gao, D. Lin, H. Liu, T. Ma, Dark photons and axion-like particles at the Electron-Ion Collider in China (12 2024). [arXiv:2412.06301](https://arxiv.org/abs/2412.06301).
- [31] B. Döbrich, J. Jaeckel, F. Kahlhoefer, A. Ringwald, K. Schmidt-Hoberg, ALPtraum: ALP production in proton beam dump experiments, *JHEP* 02 (2016) 018. [arXiv:1512.03069](https://arxiv.org/abs/1512.03069), [doi:10.1007/JHEP02\(2016\)018](https://doi.org/10.1007/JHEP02(2016)018).
- [32] M. Chala, G. Guedes, M. Ramos, J. Santiago, Running in the ALPs, *Eur. Phys. J. C* 81 (2) (2021) 181. [arXiv:2012.09017](https://arxiv.org/abs/2012.09017), [doi:10.1140/epjc/s10052-021-08968-2](https://doi.org/10.1140/epjc/s10052-021-08968-2).
- [33] F. Arias-Aragón, J. Quevillon, C. Smith, Axion-like ALPs, *JHEP* 03 (2023) 134. [arXiv:2211.04489](https://arxiv.org/abs/2211.04489), [doi:10.1007/JHEP03\(2023\)134](https://doi.org/10.1007/JHEP03(2023)134).
- [34] G. J. van Oldenborgh, J. A. M. Vermaseren, New Algorithms for One Loop Integrals, *Z. Phys. C* 46 (1990) 425–438. [doi:10.1007/BF01621031](https://doi.org/10.1007/BF01621031).
- [35] T. Hahn, M. Perez-Victoria, Automatized one loop calculations in four-dimensions and D-dimensions, *Comput. Phys. Commun.* 118 (1999) 153–165. [arXiv:hep-ph/9807565](https://arxiv.org/abs/hep-ph/9807565), [doi:10.1016/S0010-4655\(98\)00173-8](https://doi.org/10.1016/S0010-4655(98)00173-8).
- [36] M. J. Dolan, T. Ferber, C. Hearty, F. Kahlhoefer, K. Schmidt-Hoberg, Revised constraints and Belle II sensitivity for visible and invisible axion-like particles, *JHEP* 12 (2017) 094, [Erratum: *JHEP* 03, 190 (2021)]. [arXiv:1709.00009](https://arxiv.org/abs/1709.00009), [doi:10.1007/JHEP12\(2017\)094](https://doi.org/10.1007/JHEP12(2017)094).
- [37] A. Belyaev, N. D. Christensen, A. Pukhov, CalcHEP 3.4 for collider physics within and beyond the Standard Model, *Comput. Phys. Commun.* 184 (2013) 1729–1769. [arXiv:1207.6082](https://arxiv.org/abs/1207.6082), [doi:10.1016/j.cpc.2013.01.014](https://doi.org/10.1016/j.cpc.2013.01.014).
- [38] J. P. Lees, et al., Search for Invisible Decays of a Dark Photon Produced in  $e^+e^-$  Collisions at BaBar, *Phys. Rev. Lett.* 119 (13) (2017) 131804. [arXiv:1702.03327](https://arxiv.org/abs/1702.03327), [doi:10.1103/PhysRevLett.119.131804](https://doi.org/10.1103/PhysRevLett.119.131804).
- [39] E. Izaguirre, G. Krnjaic, P. Schuster, N. Toro, Testing GeV-Scale Dark Matter with Fixed-Target Missing Momentum Experiments, *Phys. Rev. D* 91 (9) (2015) 094026. [arXiv:1411.1404](https://arxiv.org/abs/1411.1404), [doi:10.1103/PhysRevD.91.094026](https://doi.org/10.1103/PhysRevD.91.094026).
- [40] E. Cortina Gil, et al., Measurement of the very rare  $K^+ \rightarrow \pi^+ \nu \bar{\nu}$  decay, *JHEP* 06 (2021) 093. [arXiv:2103.15389](https://arxiv.org/abs/2103.15389), [doi:10.1007/JHEP06\(2021\)093](https://doi.org/10.1007/JHEP06(2021)093).

- [41] Y. M. Andreev, et al., Probing light dark matter with positron beams at NA64, *Phys. Rev. D* 109 (3) (2024) L031103. [arXiv:2308.15612](#), [doi:10.1103/PhysRevD.109.L031103](#).
- [42] A. Antonov, P. Bisio, M. Bondì, A. Celentano, A. Marini, L. Marsicano, The POKERINO prototype, *Nucl. Instrum. Meth. A* 1066 (2024) 169625. [doi:10.1016/j.nima.2024.169625](#).
- [43] L. Marsicano, M. Battaglieri, M. Bondì, C. D. R. Carvajal, A. Celentano, M. De Napoli, R. De Vita, E. Nardi, M. Raggi, P. Valente, Novel Way to Search for Light Dark Matter in Lepton Beam-Dump Experiments, *Phys. Rev. Lett.* 121 (4) (2018) 041802. [arXiv:1807.05884](#), [doi:10.1103/PhysRevLett.121.041802](#).
- [44] P. Schuster, N. Toro, K. Zhou, Probing invisible vector meson decays with the NA64 and LDMX experiments, *Phys. Rev. D* 105 (3) (2022) 035036. [arXiv:2112.02104](#), [doi:10.1103/PhysRevD.105.035036](#).
- [45] Y. M. Andreev, et al., Search for pseudoscalar bosons decaying into  $e^+e^-$  pairs in the NA64 experiment at the CERN SPS, *Phys. Rev. D* 104 (11) (2021) L111102. [arXiv:2104.13342](#), [doi:10.1103/PhysRevD.104.L111102](#).
- [46] E. M. Riordan, et al., A Search for Short Lived Axions in an Electron Beam Dump Experiment, *Phys. Rev. Lett.* 59 (1987) 755. [doi:10.1103/PhysRevLett.59.755](#).
- [47] A. Konaka, et al., Search for Neutral Particles in Electron Beam Dump Experiment, *Phys. Rev. Lett.* 57 (1986) 659. [doi:10.1103/PhysRevLett.57.659](#).
- [48] M. Davier, H. Nguyen Ngoc, An Unambiguous Search for a Light Higgs Boson, *Phys. Lett. B* 229 (1989) 150–155. [doi:10.1016/0370-2693\(89\)90174-3](#).
- [49] A. Anastasi, et al., Limit on the production of a low-mass vector boson in  $e^+e^- \rightarrow U\gamma$ ,  $U \rightarrow e^+e^-$  with the KLOE experiment, *Phys. Lett. B* 750 (2015) 633–637. [arXiv:1509.00740](#), [doi:10.1016/j.physletb.2015.10.003](#).
- [50] J. R. Batley, et al., Search for the dark photon in  $\pi^0$  decays, *Phys. Lett. B* 746 (2015) 178–185. [arXiv:1504.00607](#), [doi:10.1016/j.physletb.2015.04.068](#).
- [51] D. Banerjee, et al., Improved limits on a hypothetical X(16.7) boson and a dark photon decaying into  $e^+e^-$  pairs, *Phys. Rev. D* 101 (7) (2020) 071101. [arXiv:1912.11389](#), [doi:10.1103/PhysRevD.101.071101](#).
- [52] J. P. Lees, et al., Search for a dark photon in  $e^+e^-$  collisions at BaBar, *Phys. Rev. Lett.* 113 (2014) 201801. [arXiv:1406.2980](#), [doi:10.1103/PhysRevLett.113.201801](#).
- [53] G. Abbiendi, et al., Multiphoton production in  $e^+e^-$  collisions at  $s^{*1/2} = 181\text{-GeV}$  to  $209\text{-GeV}$ , *Eur. Phys. J. C* 26 (2003) 331–344. [arXiv:hep-ex/0210016](#), [doi:10.1140/epjc/s2002-01074-5](#).
- [54] D. Banerjee, J. Bernhard, V. E. Burtsev, A. G. Chumakov, D. Cooke, P. Crivelli, E. Depero, A. V. Dermenev, S. V. Donskov, R. R. Dusaev, T. Enik, N. Charitonidis, A. Feshchenko, V. N. Frolov, A. Gardikiotis, S. G. Gerassimov, S. N. Gninenko, M. Hösken, M. Jeckel, V. A. Kachanov, A. E. Karneyeu, G. Kekelidze, B. Ketzer, D. V. Kirpichnikov, M. M. Kirsanov, V. N. Kolosov, I. V. Konorov, S. G. Kovalenko, V. A. Kramarenko, L. V. Kravchuk, N. V. Krasnikov, S. V. Kuleshov, V. E. Lyubovitskij, V. Lysan, V. A. Matveev, Y. V. Mikhailov, L. Molina Bueno, D. V. Peshekhonov, V. A. Polyakov, B. Radics, R. Rojas, A. Rubbia, V. D. Samoylenko, H. Sieber, D. Shchukin, V. O. Tikhomirov, I. Tlisova, D. A. Tlisov, A. N. Toropin, A. Y. Trifonov, B. I. Vasilishin, G. Vasquez Arenas, P. V. Volkov, V. Y. Volkov, P. Ulloa, [Search for axionlike and scalar particles with the na64 experiment](#), *Phys. Rev. Lett.* 125 (2020) 081801. [doi:10.1103/PhysRevLett.125.081801](#)  
URL <https://link.aps.org/doi/10.1103/PhysRevLett.125.081801>
- [55] A. Berlin, N. Blinov, G. Krnjaic, P. Schuster, N. Toro, [Dark matter, millicharges, axion and scalar particles, gauge bosons, and other new physics with ldmx](#), *Phys. Rev. D* 99 (2019) 075001. [doi:10.1103/PhysRevD.99.075001](#)  
URL <https://link.aps.org/doi/10.1103/PhysRevD.99.075001>
- [56] B. Batell, M. Pospelov, A. Ritz, Probing a Secluded U(1) at B-factories, *Phys. Rev. D* 79 (2009) 115008. [arXiv:0903.0363](#), [doi:10.1103/PhysRevD.79.115008](#).



- [57] P. Ciafaloni, G. Martelli, M. Raggi, Searching for dark sectors in multi lepton final state in  $e^+e^-$  collisions, JHEP 04 (2021) 163. [arXiv:2012.04754](#), [doi:10.1007/JHEP04\(2021\)163](#).
- [58] J. P. Lees, et al., Search for Low-Mass Dark-Sector Higgs Bosons, Phys. Rev. Lett. 108 (2012) 211801. [arXiv:1202.1313](#), [doi:10.1103/PhysRevLett.108.211801](#).
- [59] I. Jaegle, Search for the dark photon and the dark Higgs boson at Belle, Phys. Rev. Lett. 114 (21) (2015) 211801. [arXiv:1502.00084](#), [doi:10.1103/PhysRevLett.114.211801](#).
- [60] B. Döbrich, J. Jaeckel, T. Spadaro, Light in the beam dump - ALP production from decay photons in proton beam-dumps, JHEP 05 (2019) 213, [Erratum: JHEP 10, 046 (2020)]. [arXiv:1904.02091](#), [doi:10.1007/JHEP05\(2019\)213](#).
- [61] B. G. W., et al., Final report of the e821 muon anomalous magnetic moment measurement at bnl, Phys. Rev. D 73 (2006) 072003. [doi:10.1103/PhysRevD.73.072003](#).  
URL <https://link.aps.org/doi/10.1103/PhysRevD.73.072003>
- [62] A. D. P., et al., Measurement of the positive muon anomalous magnetic moment to 0.20 ppm, Phys. Rev. Lett. 131 (2023) 161802. [doi:10.1103/PhysRevLett.131.161802](#).  
URL <https://link.aps.org/doi/10.1103/PhysRevLett.131.161802>
- [63] A. Anastasi, et al., Combination of KLOE  $\sigma(e^+e^- \rightarrow \pi^+\pi^-\gamma(\gamma))$  measurements and determination of  $a_\mu^{\pi^+\pi^-}$  in the energy range  $0.10 < s < 0.95 \text{ GeV}^2$ , JHEP 03 (2018) 173. [arXiv:1711.03085](#), [doi:10.1007/JHEP03\(2018\)173](#).
- [64] B. Aubert, et al., Precise measurement of the  $e^+e^- \rightarrow \pi^+\pi^-(\gamma)$  cross section with the Initial State Radiation method at BABAR, Phys. Rev. Lett. 103 (2009) 231801. [arXiv:0908.3589](#), [doi:10.1103/PhysRevLett.103.231801](#).
- [65] J. P. Lees, et al., Precise Measurement of the  $e^+e^- \rightarrow \pi^+\pi^-(\gamma)$  Cross Section with the Initial-State Radiation Method at BABAR, Phys. Rev. D 86 (2012) 032013. [arXiv:1205.2228](#), [doi:10.1103/PhysRevD.86.032013](#).
- [66] L. Darmé, G. Grilli di Cortona, E. Nardi, The muon  $g - 2$  anomaly confronts new physics in  $e$  and  $\mu$  final states scattering, JHEP 06 (2022) 122. [arXiv:2112.09139](#), [doi:10.1007/JHEP06\(2022\)122](#).
- [67] L. Darmé, G. Grilli di Cortona, E. Nardi, Indirect new physics effects on  $\sigma_{\text{had}}$  confront the  $(g-2)_\mu$  window discrepancies and the CMD-3 result, Phys. Rev. D 108 (9) (2023) 095056. [arXiv:2212.03877](#), [doi:10.1103/PhysRevD.108.095056](#).
- [68] F. V. Ignatov, et al., Measurement of the  $e^+e^- \rightarrow \pi^+\pi^-$  cross section from threshold to 1.2 GeV with the CMD-3 detector, Phys. Rev. D 109 (11) (2024) 112002. [arXiv:2302.08834](#), [doi:10.1103/PhysRevD.109.112002](#).
- [69] B. Ward, S. Jadach, Z. Was, Precision calculation for  $e^+e^- \rightarrow 2f$ : the  $kk \text{ mc}$  project, Nuclear Physics B - Proceedings Supplements 116 (2003) 73–77. [doi:10.1016/S0920-5632\(03\)80147-0](#).  
URL [http://dx.doi.org/10.1016/S0920-5632\(03\)80147-0](http://dx.doi.org/10.1016/S0920-5632(03)80147-0)
- [70] N. Amapane, et al., Study of muon pair production from positron annihilation at threshold energy, JINST 15 (01) (2020) P01036. [arXiv:1909.13716](#), [doi:10.1088/1748-0221/15/01/P01036](#).
- [71] P. Zyla, et al., Review of Particle Physics, PTEP 2020 (8) (2020) 083C01, and 2021 update. [doi:10.1093/ptep/ptaa104](#).
- [72] S. J. Brodsky, R. F. Lebed, Production of the Smallest QED Atom: True Muonium ( $\mu^+\mu^-$ ), Phys. Rev. Lett. 102 (2009) 213401. [arXiv:0904.2225](#), [doi:10.1103/PhysRevLett.102.213401](#).
- [73] H. Lamm, Hadronic vacuum polarization in true muonium, Phys. Rev. A 95 (2017) 012505. [doi:10.1103/PhysRevA.95.012505](#).  
URL <https://link.aps.org/doi/10.1103/PhysRevA.95.012505>

- [74] Lamm, Henry, Ji, Yao, [Predicting and discovering true muonium \( \$\mu^+\mu^-\$ \)](#), EPJ Web of Conferences 181 (2018) 01016. doi:[10.1051/epjconf/201818101016](https://doi.org/10.1051/epjconf/201818101016).  
URL <https://doi.org/10.1051/epjconf/201818101016>
- [75] X. C. Vidal, P. Ilten, J. Plews, B. Shuve, Y. Soreq, [Discovering true muonium at LHCb](#), Physical Review D 100 (5) (sep 2019). doi:[10.1103/physrevd.100.053003](https://doi.org/10.1103/physrevd.100.053003).  
URL <https://doi.org/10.1103/physrevd.100.053003>
- [76] J. Sonneveld, Its3: A truly cylindrical inner tracker for alice (2023). [arXiv:2307.08632](https://arxiv.org/abs/2307.08632).